To restore baseline spiking while the endogenous SK current was blocked with apamin, we adjusted the parameters that described the artificial SK current applied with dynamic clamping (see Methods section). Figure 3C shows that the artificial SK current (20–50 pA) restored regular single spiking. Further, when the current injection was removed, irregular bursting reappeared immediately.

In control and SK current injection conditions [Fig. 4A(a) and (b), respectively], positive correlations were observed between the negative peak after each spike and the spontaneous spike rate of the DA neurons. This indicates that spike frequency was controlled by the SK current, as reported by Feng and Jaeger [26] for neurons of deep cerebellar nuclei. Figure 4A(c) shows that, in some DA neurons (eight of 12 cells), an artificial SK current injection slightly increased spontaneous firing. This observation may be related to the fact that the restored negative peak voltage after spikes was slightly higher than that observed without the SK current injection.

The recovery of regular spiking in the presence of apamin depended on both the extent of irregular bursting and the injected SK current. As shown in Fig. 3D, longer periods of bursting required an SK current between 50 and 100 pA. In all of the tested cases ($n = 12$), the application of the artificial SK current during an apamin-induced bursting led to regular spiking. Therefore, the coefficients of variation of the ISIs in the presence of apamin were reduced to the control level (0.1–0.2) if the SK conductance was adjusted to an appropriate cell-specific value. Figure 4B shows that single-spike activity and regularity recovered when the SK values were adjusted.

A calcium concentration decay time constant between 20 and 35 ms was able to restore the time course of the AHPs. Decays in the calcium levels have been directly measured after evoking single spikes in response to a briefly (30–50 ms) injected step current. The average value of the decay time constant was $34.3 \pm 8.0$ ms ($n = 5$) immediately after the cell membrane was broken. Therefore, the result was consistent with those obtained in the SK current injection experiments, although the measured average value was slightly larger than that used in the model.

## Discussion

Here, we reported a new dynamic clamp technique in which $Ca^{2+}$ levels were used to adjust a conventional dynamic clamp protocol. With the technique, we estimated the injected SK current from both directly measured $Ca^{2+}$-derived fluorescence signals and a mathematical model of intracellular $Ca^{2+}$ dynamics. This approach enabled us to test our mathematical models in real time by observing the neurons' firing modes and spike properties.

**Fig. 4**

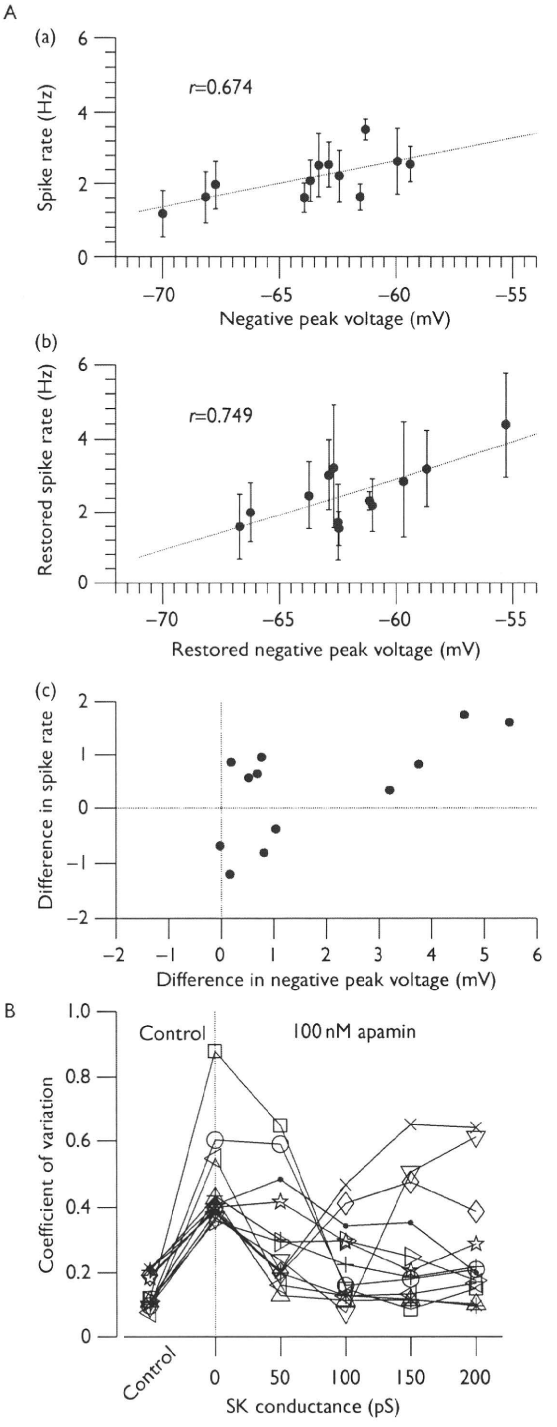


A, (a) Spike statistics before and after small-conductance (SK) current was injected while the endogenous SK current was blocked. Positive correlations were observed between the negative peak voltages after spikes and the spontaneous firing rate (a) before SK current block and (b) after an artificial SK current was injected. The correlation coefficients ($r$) are indicated. (c) The relationships between the original and the recovered negative peak voltages and the firing rate are shown ($n = 12$ cells). B, Variable or consistent spiking in control samples, or in the presence or absence of injected SK current. Coefficients of variation (SD/mean) for the interspike intervals are plotted.

DA neurons showed several typical firing modes *in vivo*, including burst activity and low-frequency tonic firing (< 10 Hz) with regular or irregular patterns. In contrast, DA cells *in vitro* fire autonomously and tonically with a regular pattern. The calcium current that mediates the autonomous regular firing is likely, at least partly carried by L-type $Ca^{2+}$ channels, because it is inhibited by L-type channel blockers, but not N-type channel blockers [6,9,15]. Although the effects of P/Q-type channel blockers on this activity have not yet been determined *in vivo*, Puopolo *et al.* [15] showed that a selective P-type channel blocker markedly inhibited firing in the midbrain slices. Treatment of DA neurons in these brain slice preparations with apamin shifted the firing mode from a regular firing pattern to a burst pattern. In DA cells, therefore, the firing mode and action potential frequency and initiation are regulated by an SK $Ca^{2+}$-dependent $K^+$ current.

We showed that the SK current in DA neurons partly accounts for the AHP and contributes to the regularity of the ISIs. Our results also showed that, in response to the current injection under baseline conditions, the AHP is the predominant regulator of the spike frequency. A recent study showed that the SK current in DA neurons is primarily the result of inflow through T-type and N-type channels together with minor contributions from several other calcium currents [13]. In this study, we applied an artificial SK current with dynamic clamping using four types of $Ca^{2+}$ current as the calcium source. The results revealed that pulsatile calcium inflow after each spike and subsequent calcium decay with a time constant ranging from 20 to 35 ms could explain the observed AHP properties. As indicated in other studies [26], the decay of the intracellular calcium pool may represent the short period of time for which the SK channels are exposed to an elevated calcium concentration at the membrane. Thus, the short exposure may allow intracellular calcium to accumulate without elevation of the SK current.

The minimum artificial SK current amplitude that was required to eliminate irregular and burst spiking was such that the ensuing AHP had a slightly larger amplitude than that recorded during the baseline activity. This, however, did not necessarily slow the recovery of regular spiking compared with the pre-apamin treatment condition. Rather, at times, it accelerated regular spontaneous firing in the tested DA neurons [Fig. 3A(c)]. This observation may be associated with the rapid recovery of a spike refractory period, which always occurred when the inhibitory synaptic input was injected. We showed that certain SK values promoted regular ISIs in the DA neurons. This value needed to be adjusted to restore regular tonic firing in the presence of apamin, because the appropriate value was cell specific. Although the maximum injected current amplitude was 50 pA, the time course of the injected current was critical to control the firing mode.

Calcium signals generated by voltage-dependent $Ca^{2+}$ channels may be amplified by secondary calcium release from intracellular stores, which has also been shown to activate SK channels. Indeed, SK channels in the DA neurons can be activated by the intracellular calcium release evoked through metabotropic glutamate receptors [27]. This secondary calcium release may contribute to the discrepancy observed in the latter portions of the $[Ca^{2+}]_i$ time courses obtained using $Ca^{2+}$-derived fluorescence signals and numerical simulation with our model [see Fig. 1B(b) and C(b)].

Recent studies have shown that the midbrain DA neurons are a heterogeneous population of neurons and that there is a media-lateral gradient in SK3 channel expression [28]. However, in the presence of apamin, we could not find any differences between the recorded DA neurons in the SNc and those in the lateral part of the VTA. The reason for this may be that the number of sampled VTA DA neurons was small (eight cells) and they were located in the lateral part of the VTA in which the SK3 channels are highly expressed [28].

Ji and Shepard [29] reported that local and systemic administration of apamin increases the incidence and intensity of the bursting activity among the DA neurons recorded in intact rats. However, they also pointed out that, consistent with its effects in brain slices, the ability of apamin to increase bursting activity *in vivo* could not have been simply presupposed. Pacemaker activity exhibited by the DA neurons *in vitro* or pacing with a scale of high precision such that the coefficient of variation in the interspike intervals is less than 12%, is rarely observed *in vivo*, where the continuum of the patterned activity is often attributed to synaptic inputs. Therefore, in addition to the mechanism involving SK channels, DA cells also require *N*-methyl-D-aspartate (NMDA) receptor-gated channels for burst activity. Under certain in-vivo conditions, either or both of these mechanisms could induce burst firing. NMDA receptor-mediated burst firing would be induced by inputs from glutamate-containing synaptic connections. The approach presented here may help elucidate these mechanisms, because the dynamic clamp technique can be used to mimic NMDA-like synaptic inputs.

## Conclusion

To test the validity of a $Ca^{2+}$-dependent $K^+$ current model in in-vitro preparations of DA neurons in the SNc and the lateral part of the VTA, we developed a new dynamic clamp technique in which fluorescence imaging of $Ca^{2+}$ levels was incorporated into a conventional dynamic clamp protocol. As reported before, our experimental results combined with mathematical modeling indicate that an SK $Ca^{2+}$-dependent $K^+$ current markedly shapes the firing modes and spike properties of these neurons. In addition, our results support the fact that the

measurement of intracellular $Ca^{2+}$ level can be possibly replaced with the calcium dynamics model as an input to the dynamic clamp system.

## Acknowledgements

Grant support: Precursory research for Embryonic Science and Technology (PRESTO), Japan Science and Technology Agency (JST). Grant-in-Aid for Scientific Research (B) and Exploratory Research, the Ministry of Education, Culture, Sports, Science and Technology (MEXT).

## References

1 Schultz W. Getting formal with dopamine and reward. *Neuron* 2002; **36**:241–263.
2 Brozoski TJ, Brown RM, Rosvold HE, Goldman PS. Cognitive deficit caused by regional depletion of dopamine in prefrontal cortex of rhesus monkey. *Science* 1979; **205**:929–932.
3 Graybiel AM, Aosaki T, Flaherty AW, Kimura M. The basal ganglia and adaptive motor control. *Science* 1994; **265**:1826–1831.
4 Liss B, Roeper J. Individual dopamine midbrain neurons: functional diversity and flexibility in health and disease. *Brain Res Rev* 2008; **58**:314–321.
5 Durante P, Cardenas CG, Whittaker JA, Kitai ST, Scroggs RS. Low-threshold L-type calcium channels in rat dopamine neurons. *J Neurophysiol* 2004; **91**:1450–1454.
6 Nedergaard S, Flatman JA, Engberg I. Nifedipine- and omega-conotoxin-sensitive $Ca^{2+}$ conductances in guinea-pig substantia nigra pars compacta neurones. *J Physiol* 1993; **466**:727–747.
7 Chan CS, Guzman JN, Ilijic E, Mercer JN, Rick C, Tkatch T, *et al.* Rejuvenation protects neurons in mouse models of Parkinson's disease. *Nature* 2007; **447**:1081–1086.
8 Kang Y, Kitai ST. A whole cell patch-clamp study on the pacemaker potential in dopaminergic neurons of rat substantia nigra compacta. *Neurosci Res* 1993; **18**:209–221.
9 Mercuri NB, Bonci A, Calabresi P, Stratta F, Stefani A, Bernardi G. Effects of dihydropyridine calcium antagonists on rat midbrain dopaminergic neurones. *Br J Pharmacol* 1994; **113**:831–838.
10 Xu W, Lipscombe D. Neuronal Ca(V)1.3alpha(1) L-type channels activate at relatively hyperpolarized membrane potentials and are incompletely inhibited by dihydropyridines. *J Neurosci* 2001; **21**:5944–5951.
11 Ping HX, Shepard PD. Apamin-sensitive Ca(2+)-activated K+ channels regulate pacemaker activity in nigral dopamine neurons. *Neuroreport* 1996; **7**:809–814.
12 Shepard PD, Bunney BS. Repetitive firing properties of putative dopamine-containing neurons in vitro: regulation by an apamin-sensitive Ca(2+)-activated K+ conductance. *Exp Brain Res* 1991; **86**:141–150.
13 Wolfart J, Roeper J. Selective coupling of T-type calcium channels to SK potassium channels prevents intrinsic bursting in dopaminergic midbrain neurons. *J Neurosci* 2002; **22**:3404–3413.
14 Faber ESL. Functions and modulation of neuronal SK channels. *Cell Biochem Biophys* 2009; **55**:127–139.
15 Puopolo M, Raviola E, Bean BP. Roles of subthreshold calcium current and sodium current in spontaneous firing of mouse midbrain dopamine neurons. *J Neurosci* 2007; **27**:645–656.
16 Johnson SW, Wu YN. Multiple mechanisms underlie burst firing in rat midbrain dopamine neurons in vitro. *Brain Res* 2004; **1019**:293–296.
17 Robinson HP, Kawai N. Injection of digitally synthesized synaptic conductance transients to measure the integrative properties of neurons. *J Neurosci Methods* 1993; **49**:157–165.
18 Sharp AA, O'Neil MB, Abbott LF, Marder E. Dynamic clamp: computer-generated conductances in real neurons. *J Neurophysiol* 1993; **69**:992–995.
19 Destexhe A, Rudolph M, Fellous JM, Sejnowski TJ. Fluctuating synaptic conductances recreate in vivo-like activity in neocortical neurons. *Neuroscience* 2001; **107**:13–24.
20 Sieling FH, Canavier CC, Prinz AA. Predictions of phase-locking in excitatory hybrid networks: excitation does not promote phase-locking in pattern-generating networks as reliably as inhibition. *J Neurophysiol* 2009; **102**:69–84.
21 Grynkiewicz G, Poenie M, Tsien RY. A new generation of $Ca^{2+}$ indicators with greatly improved fluorescence properties. *J Biol Chem* 1985; **260**:3440–3450.
22 Wilson CJ, Callaway JC. Coupled oscillator model of the dopaminergic neuron of the substantia nigra. *J Neurophysiol* 2000; **83**:3084–3100.
23 Foehring RC, Zhang XF, Lee JC, Callaway JC. Endogenous calcium buffering capacity of substantia nigral dopamine neurons. *J Neurophysiol* 2009; **102**:2326–2333.
24 Amini B, Clark JW Jr, Canavier CC. Calcium dynamics underlying pacemaker-like and burst firing oscillations in midbrain dopaminergic neurons: a computational study. *J Neurophysiol* 1999; **82**:2249–2261.
25 Canavier CC, Oprisan SA, Callaway JC, Ji H, Shepard PD. Computational model predicts a role for ERG current in repolarizing plateau potentials in dopamine neurons: implications for modulation of neuronal activity. *J Neurophysiol* 2007; **98**:3006–3022.
26 Feng SS, Jaeger D. The role of SK calcium-dependent potassium currents in regulating the activity of deep cerebellar nucleus neurons: a dynamic clamp study. *Cerebellum* 2008; **7**:542–546.
27 Morikawa H, Imani F, Khodakhah K, Williams JT. Inositol 1,4,5-triphosphate-evoked responses in midbrain dopamine neurons. *J Neurosci* 2000; **20**:RC103.
28 Sarpal D, Koenig JI, Adelman JP, Brady D, Prendeville LC, Shepard PD. Regional distribution of SK3 mRNA-containing neurons in the adult and adolescent rat ventral midbrain and their relationship to dopamine-containing cells. *Synapse* 2004; **53**:104–113.
29 Ji H, Shepard PD. SK $Ca^{2+}$-activated $K^+$ channel ligands alter the firing pattern of dopamine-containing neurons in vivo. *Neuroscience* 2006; **140**:623–633.

Sensors and Actuators A 158 (2010) 183–192

Contents lists available at ScienceDirect

Sensors and Actuators A: Physical

journal homepage: www.elsevier.com/locate/sna

# Development of piezoelectric acoustic sensor with frequency selectivity for artificial cochlea

Hirofumi Shintaku[a,*], Takayuki Nakagawa[b], Dai Kitagawa[a], Harto Tanujaya[a], Satoyuki Kawano[a], Juichi Ito[b]

[a] Department of Mechanical Science and Bioengineering, Graduate School of Engineering Science, Osaka University, Machikaneyama-cho 1-3, Toyonaka, Osaka 560-8531, Japan
[b] Department of Otolaryngology, Head and Neck Surgery, Graduate School of Medicine, Kyoto University, Kawahara-cho 54,Shogoin, Sakyo-ku, Kyoto 606-8507, Japan

ARTICLE INFO

*Article history:*
Received 25 July 2009
Received in revised form
13 November 2009
Accepted 22 December 2009
Available online 4 January 2010

*Keywords:*
Fluid-structure interaction
Acoustic MEMS sensor
Artificial cochlea
Biomechanical engineering
Piezoelectric device

ABSTRACT

In this paper, we report a novel piezoelectric artificial cochlea which realizes both acoustic/electric conversion and frequency selectivity without an external energy supply. The device comprises an artificial basilar membrane (ABM) which is made of a 40 μm thick polyvinylidine difluoride (PVDF) membrane fixed on a substrate with a trapezoidal slit. The ABM over the slit, which mimics the biological system, is vibrated by acoustic waves and generates electric output due to the piezoelectric effect of PVDF. The width of ABM is linearly varied from 2.0 to 4.0 mm along the longitudinal direction of 30 mm to change its local resonant frequency with respect to the position. A detecting electrode array with 24-elements of 0.50 × 1.0 mm rectangles is made of an aluminum thin film on ABM, where they are located in a center line of longitudinal direction with the gaps of 0.50 mm. Since the device will be implanted into a cochlea filled with lymph fluid in future, the basic characteristics in terms of vibration and acoustic/electric conversion are investigated both in the air and in the silicone oil which is a model of lymph fluid. The in vitro optical measurements show that the local resonant frequency of vibration is varied along the longitudinal direction from 6.6 to 19.8 kHz in the air and from 1.4 to 4.9 kHz in the silicone oil, respectively. Since a resonating place vibrates with relatively large amplitude, the electric output there becomes high and that at the other electrodes remains to be low. Thus, the electric voltages from each electrode realize the frequency selectivity. Furthermore, the effect of surrounding fluid on the vibration is discussed in detail by comparing the experimental results with the theoretical predictions obtained by the Wentzel–Kramers–Brillouin asymptotic method. The theoretical prediction indicates that the surrounding fluid of the higher density induces the larger effective mass for the vibration that results in lower resonant frequency. From these findings, the feasibility of artificial cochlea is confirmed both experimentally and theoretically.



## 1. Introduction

The sensorineural hearing loss is a type of deafness which is often caused by the damage on hair cells of cochleae in inner ears. The hair cells convert acoustic sounds to electric signals that stimulate auditory nerves. As a clinical treatment for the hearing loss in children and adults, the artificial cochlea is recently well used. The device bypasses the damaged hair cells by generating the electric current in response to the acoustic sound [1,2]. The current artificial cochlea consists of an implantable electrode array for the stimulation and an extracorporeal device including a microphone, a sound processor and a battery. The acoustic sound is detected and is analyzed with respect to the frequency by the extracorporeal device. The processed signals are transferred through a transcutaneous system. Then, the auditory nerves are stimulated through the electrodes inserted in the cochlea. The disadvantages in the current system are the indispensability of extracorporeal devices, the small number of electrodes which closely connects to the limitation of tones, and the relatively large power consumption. This situation motivates us to develop a fully self-contained implantable artificial cochlea.

The important functions of cochlea are not only the conversion of acoustic wave to electric signals but also the frequency selectivity [3,4]. The basilar membrane which is a biological diaphragm in the cochlea plays an important role for the frequency selectivity. The local eigen frequency of membrane is changing along the place

* Corresponding author. Tel.: +81 6 6850 6179; fax: +81 6 6850 6179.
*E-mail address:* shintaku@me.es.osaka-u.ac.jp (H. Shintaku).

0924-4247/$ – see front matter © 2009 Elsevier B.V. All rights reserved.
doi:10.1016/j.sna.2009.12.021

**Nomenclature**

| | |
|---|---|
| $A_j$ | Fourier coefficient |
| $b(x)$ | width of ABM, m |
| $D$ | bending rigidity, N m |
| $E$ | Young's modulus, Pa |
| $f$ | frequency, Hz |
| $h$ | thickness of ABM, m |
| $k(x)$ | wave number, $m^{-1}$ |
| $L_1$ | width of fluid channel, m |
| $L_2$ | depth of fluid channel, m |
| $L_3$ | length of ABM, m |
| $p_f$ | pressure, Pa |
| $w$ | displacement of ABM, m |
| $W(x)$ | envelope function, m |
| $(x, y, z)$ | Cartesian coordinates, m |

*Greek letters*

| | |
|---|---|
| $\eta(x, y)$ | shape function for ABM's bending in $y$ direction |
| $\nu$ | Poisson ratio |
| $\rho_f$ | density of fluid, kg $m^{-3}$ |
| $\rho_m$ | density of PVDF, kg $m^{-3}$ |
| $\phi_f(x, y, z, t)$ | velocity potential, $m^2/s$ |
| $\omega$ | angular frequency, rad/s |

*Subscripts*

| | |
|---|---|
| f | region of fluid channel f = l or u |
| j | mode number of Fourier coefficient |
| l | lower fluid channel |
| m | PVDF |
| u | upper fluid channel |

of it, because of varying mechanical boundary conditions and the mechanical rigidity. Thus, when the eigen frequency at a local place match to that of acoustic wave, the place vibrates with relatively large amplitude due to the resonance. The vibration stimulates hair cells especially at the resonated place. As a result, the frequency of acoustic wave is recognized as the difference in tones.

To artificially realize the frequency selectivity, some microscaled devices have been reported. Tanaka et al. [5] and Xu et al. [6] developed acoustic sensors with the function of frequency selectivity by the use of resonance of cantilever arrays. Those sensors were evaluated in the atmospheric environment. Chen et al. [7] developed a beam array fixed on a trapezoidal channel and investigated the vibrating characteristics in the water. Despite the frequency selectivity of cantilevers or beams, their mechanical strength may not be enough for the implantation as the artificial cochleae for the long period. On the other hand, White and Grosh [8] developed a device made of polyimide membrane with $Si_3N_4$ beams. The demonstration for the frequency selectivity was conducted at the higher frequency range compared with the audible one. Wittbrodt et al. [9] also developed a device made of polyimide membrane with Al beams. They reported that the device possessed some similarities with the biological cochlea in terms of traveling waves, the frequency to place tonotopic organization, and the roll off beyond the characteristic place.

The acoustic sensor which is developed in this paper realizes both the frequency selectivity and the conversion of acoustic wave to the electric signal in the liquid environment without an external energy supply. The device is designed as a prototype model to test the basic concept of the acoustic sensor for the development of the self-contained implantable artificial cochlea. The device consists of a piezoelectric membrane fixed on a trapezoidal slit, where the membrane over the slit works as a detector. We name this trapezoidal membrane as an artificial basilar membrane (ABM). Discrete electrodes are fabricated on ABM by technologies of micro electromechanical systems (MEMS) to measure the electric signals generated in response to the externally applied acoustic waves. To model the liquid environment, the fluid channel which locates under ABM is filled with a silicone oil as a model of lymph fluid in the cochlea. The ABM's vibration is measured using a laser Doppler vibrometer (LDV) at the various frequencies in the range of 1.0–20 kHz. The electric output is measured through the electrodes using a preamplifier. To predict the performance of the present device, the oscillatory dynamics of ABM is theoretically analyzed based on the vibrating equation of a thin plate bending and equations for the fluid dynamics. The phenomenon of fluid-structure interaction is treated by coupling those basic equations. To treat the wave motion on trapezoidal ABM, the Wentzel–Kramers–Brillouin (WKB) asymptotic solution [10] is used under the assumption of the gradually varying wavelength. The comparison between the experimental and theoretical results makes clear the detailed mechanism underlying the frequency selectivity. In addition, discussions for the further development as an implantable artificial cochlea are described from the viewpoint of magnitude of electric signal and the device size.

## 2. Principles and experimental methods

### 2.1. Basic mechanism of frequency selectivity and electric signal generation

A schematic and a photograph of piezoelectric acoustic sensor developed here are shown in Fig. 1. The device comprises a polyvinylidine difluoride (PVDF) membrane (KUREHA, Japan) bonded on a stainless plate with a trapezoidal slit and discrete electrodes distributed along $x$ axis. PVDF is a piezoelectric material which can convert mechanical stresses to electric signals. The trapezoidal slit is designed so that the membrane over it, i.e. ABM, can be easily vibrated by the acoustic wave. The width $b(x)$ of ABM is linearly varied in the ranges of 2.0–4.0 mm along $x$ of 30 mm long. This shape is intended to mimic the passive basilar membrane, that is, the local resonant frequency (LRF) of ABM gradually changes due to the varying mechanical boundary conditions along $x$. LRF is expected to be decreased as $x$ increases. Applying acoustic wave with a certain frequency to ABM, a local place vibrates with relatively large amplitude due to the resonance. Electric signals are generated by the piezoelectric effect with respect to the local stress in ABM. Thus, the electrode on the resonating place gives a relatively large electric output. This is the basic mechanism of frequency selectivity realized by the association of resonance of vibration and the discrete electrode array. The device is mounted on a substrate with a fluid channel, where the channel dimensions are 47 × 17 mm rectangle and 4 mm deep. To model an in vivo environment, the fluid channel is filled with silicone oil (Shin-Etsu Chemical, Japan). The density and the viscosity of silicone oil are 873 kg/$m^3$ and 1.75 × $10^{-3}$ Pa s, respectively, where those of lymph fluid in cochleae are typically reported as 1.0 × $10^3$ kg/$m^3$ [11] and from 1.0 × $10^{-3}$ to 1.97 × $10^{-3}$ Pa s [12,13], respectively. Although the both sides of basilar membrane in vivo face to the lymph fluid, in this experiment, only the bottom side of ABM faces to the silicone oil for the stable optical measurement from the upper side. The effect of this simplification is discussed by the theoretical analysis in the later section. Furthermore, the size of this ABM is relatively large to be implanted into the human cochlea. However, the main purpose of this paper is to test the basic mechanism of proposed system in terms of acoustic/electric conversion and the frequency selectivity. The optimization and the miniaturization will be remained as a future work. The advantages of miniaturized ABM are again discussed in later section.

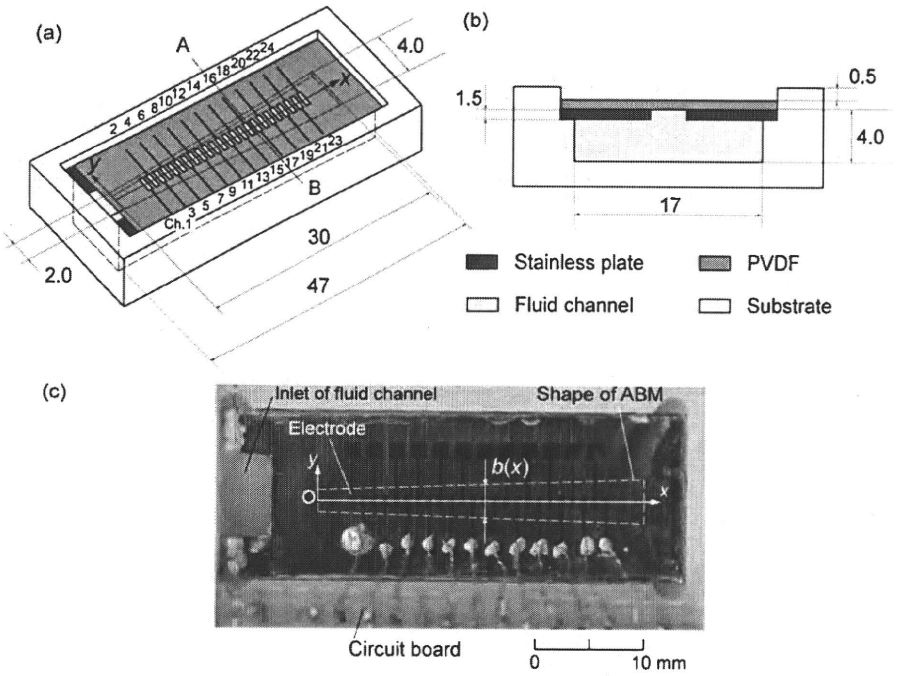


**Fig. 1.** Schematic and photograph of piezoelectric acoustic sensor; (a) 3D view, (b) cross sectional view at AB, and (c) photograph (Unit: mm).

### 2.2. Experimental setup

The electrode array with 24 elements made of an aluminum thin film is fabricated on an upper side of a 40 μm thick PVDF membrane based on a standard photolithography and an etching process. For convenience, the electrodes are named as Ch.1–Ch.24 as shown in Fig. 1(a). The each electrode of 0.50 × 1.0 mm rectangular shape is equally spaced 1.0 mm center to center, resulting in a gap of 0.50 mm between two adjacent electrodes. The ground electrode is prepared as a common one for all discrete electrodes on the lower side of ABM. The membrane is glued on the stainless plate to be the trapezoidal ABM. Since the electrodes of about 100 nm thick are extremely thinner than the PVDF of 40 μm, they may not strongly affect on the vibrating characteristics of ABM.

Fig. 2 shows a schematic of experimental setup. The sinusoidal acoustic wave is applied to the device from a speaker (FOSTEX, Japan) which is located 120 mm distant with 45° at a tilt. The speaker is previously calibrated to realize the constant sound pressure with the precision of ±0.1 dBSPL at various frequencies. The frequency is controlled by the function generator (NF, Japan) from 1.0 to 20 kHz which is in the range of audible frequency. The device on the substrate is set on a motorized stage which moves $x$ and $y$ directions for the measurement of spatial distribution of vibration amplitude. The velocity of ABM in $z$ due to the vibration by the acoustic wave is measured by the LDV (Graphtec, Japan). The displacement, which is converted from the velocity data, is analyzed by an FFT to obtain the amplitude of vibration at the frequency of acoustic wave. At the same time, the piezoelectric output from the electrodes is measured in terms of voltage using a preamplifier and an oscilloscope.

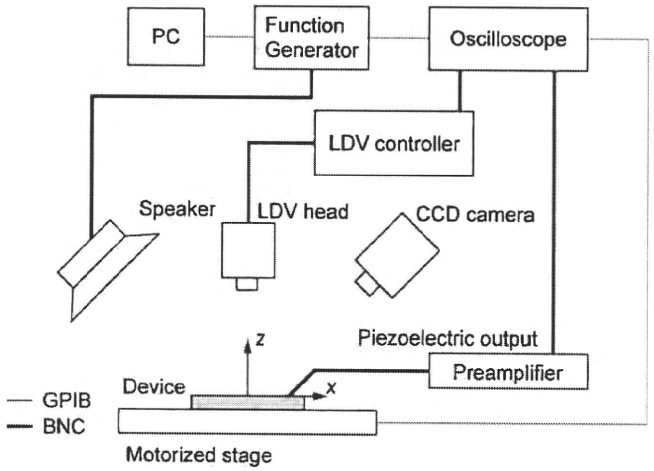


**Fig. 2.** Schematic of experimental setup for measurement of vibrating characteristics of ABM.

### 2.3. Oscillatory dynamics of artificial basilar membrane

Because the phenomena including the fluid-structure interaction are relatively complex, it is important for practical engineering to develop a theoretical model that effectively and easily predicts the vibrating characteristics of ABM. To obtain a mathematical solution, the following assumptions are made based on the experimental observations.

(1) The vibration of ABM is modeled as the bending vibration of a thin plate with small-amplitudes. The plain stress condition is valid, since the thickness $h$ of ABM is small compared with the width or length.
(2) The fluid flow is assumed as incompressible, since $O(\omega^2 L^2/c^2)$ is $10^{-2}$–$10^{-6}$, where the angular frequency $\omega$ is $O(10^3)$–$O(10^5)$, the characteristic length $L$ is $O(10^{-3})$, and the sound velocity $c$ is $O(10^3)$.
(3) The effects of gravity and viscosity of surrounding fluid are ignored.

The governing equation for the bending vibration of a plate with isotropic mechanical properties can be described as

$$\rho_m h \frac{\partial^2 w}{\partial t^2} + D\left[\frac{\partial^4 w}{\partial x^4} + 2\frac{\partial^4 w}{\partial x^2 \partial y^2} + \frac{\partial^4 w}{\partial y^4}\right] = p_0 \quad (1)$$

where $D$, $p_0$, $w$, and $\rho_m$ are the bending rigidity, the pressure of acoustic wave, the displacement in $z$ direction, and the density of ABM, respectively. The bending rigidity $D$ is related to Young's modulus $E$ as

$$D = \frac{Eh^3}{12(1-\nu^2)} \tag{2}$$

where $\nu$ is the Poisson ratio.

The basic equation for the fluid flow is the Laplace equation of velocity potential $\phi_f$ as

$$\frac{\partial^2\phi_f}{\partial x^2} + \frac{\partial^2\phi_f}{\partial y^2} + \frac{\partial^2\phi_f}{\partial z^2} = 0 \tag{3}$$

The velocity potential $\phi_f$ is related to the velocity components $(u_x, u_y, u_z)$ as

$$u_x = \frac{\partial\phi_f}{\partial x}, \quad u_y = \frac{\partial\phi_f}{\partial y}, \quad u_z = \frac{\partial\phi_f}{\partial z} \tag{4}$$

respectively. The subscript f is $u$ or $l$, where $u$ and $l$ indicate the fluid at the upper and lower sides of ABM, respectively. Furthermore, the velocity potential $\phi_f$ is related to the pressure as

$$\rho_f\frac{\partial\phi_f}{\partial t} = -p_f \tag{5}$$

where $\rho_f$ is the density of fluid.

The governing equations are solved with the following boundary conditions. The normal velocities at the wall of fluid channel are written as

$$u_z = \frac{\partial\phi_l}{\partial z} = 0 \quad \text{at} \quad z = -L_2 \tag{6}$$

$$u_y = \frac{\partial\phi_l}{\partial y} = 0 \quad \text{at} \quad y = \pm\frac{L_1}{2} \tag{7}$$

where $L_1$ and $L_2$ are the width and the depth of fluid channel, respectively. The kinematic boundary condition at $z=0$ is written as

$$\frac{\partial w}{\partial t} = \frac{\partial\phi_f}{\partial z} \quad \text{at} \quad z = 0 \tag{8}$$

The thickness $h$ of ABM is ignored in the analysis of fluid flow, since it is relatively small compared with the depth $L_2$ of fluid channel. The pressure $p_0$ is the pressure difference between the upper and lower sides of ABM and can be written as

$$p_0 = -\rho_l\frac{\partial\phi_l}{\partial t} + \rho_u\frac{\partial\phi_u}{\partial t} \quad \text{at} \quad z = 0 \tag{9}$$

Since $\rho_l$ is extremely large compared with $\rho_u$ in the present experiment, Eq. (9) is approximated as

$$p_0 \cong -\rho_l\frac{\partial\phi_l}{\partial t} \quad \text{at} \quad z = 0 \tag{10}$$

To obtain the oscillatory solution at the periodic steady state, following assumptions are made.

(4) A single mode $\eta(x, y)$ is used for the shape function of ABM's bending in $y$ direction. $\eta(x,y)$ is determined based on the analytical solution of a vibrating beam with the first mode, the length of $b(x)$, and the fixed boundary conditions at $y=\pm b(x)/2$ as

$$\eta(x,y) = \begin{cases} c_1\cos\left(\dfrac{\beta}{b(x)}y\right) + c_2\cosh\left(\dfrac{\beta}{b(x)}y\right) & \text{at} \quad -\dfrac{b(x)}{2} \le y \le \dfrac{b(x)}{2} \\ 0 \quad \text{at} \quad -\dfrac{L_1}{2} \le y \le -\dfrac{b(x)}{2} \quad \text{and} \quad \dfrac{b(x)}{2} \le y \le \dfrac{L_1}{2} \end{cases} \tag{11}$$

where $c_1$, $c_2$, and $\beta$ are constants of 0.8827, 0.1173 and 4.730, respectively. These constants are determined to make $\eta(x, y)$ satisfy the fixed boundary conditions at $y=\pm b(x)/2$.

(5) The wave is considered as a slowly varying wave in $x$ direction. That is, the wave number $k(x)$ is slowly varying along $x$ as $b(x)$, where $db(x)/dx \cong 0$ and $dk(x)/dx \cong 0$ are reasonable in the scale of a one wavelength. In this case, the waves can be treated as pseudo plane ones and can be described by the WKB asymptotic solution [10].

Based on these assumptions described above, the displacement $w(x, y, t)$ of ABM can be written as

$$w = W(x)\eta(x,y)e^{i\int_0^x k(\xi)d\xi}e^{-i\omega t} \tag{12}$$

where $i$ and $W(x)$ are the imaginary number and the envelope function, respectively. $W(x)$ is also treated as a slowly varying function, that is $dW(x)/dx \cong 0$, since the effect of $dW(x)/dx$ on the dispersion relationship is trivial for linear problems [14]. The main purpose of the theoretical analysis is to predict the distribution of the local resonant frequency and to clarify the effect of the surrounding fluid on the resonance. Therefore, to simplify the mathematical development, only the forward wave is included in the analysis. On the other hand, the solution for Eq. (3) which satisfies the boundary conditions of Eqs. (6) and (7) is written as

$$\phi_l = \sum_{j=0}^{\infty} A_j\cosh\left[\zeta_j(z+L_2)\right]\cos\left(\frac{j\pi}{L_1}y\right)e^{i\int_0^x k(\xi)d\xi}e^{-i\omega t} \tag{13}$$

where $A_j$ and $\zeta_j$ are the Fourier coefficient for jth mode and $[k^2(x)+(j\pi/L_1)^2]^{1/2}$, respectively. From Eqs. (8), (12) and (13), the following equation is obtained:

$$i\omega W(x)\eta(x,y) = -\sum_{j=0}^{\infty} A_j\zeta_j\sinh(\zeta_j L_2)\cos\left(\frac{j\pi}{L_1}y\right) \tag{14}$$

Using the orthogonality of cosine function, $A_j$ is calculated as

$$A_j = -\frac{i\omega W(x)\int_{-b(x)/2}^{b(x)/2}\eta(x,y)\cos\left(j\pi y/L_1\right)dy}{\zeta_j\sinh\left(\zeta_j L_2\right)\int_{-L_1/2}^{L_1/2}\cos^2\left(j\pi y/L_1\right)dy} \tag{15}$$

Eqs. (10) and (12) are substituted into Eq. (1). Then, multiplying $\eta(x,y)$ to Eq. (1), and integrating from $-b(x)/2$ to $b(x)/2$ with respect to $y$, the following eikonal equation is obtained:

$$\begin{aligned} f(x,\omega) &= D\left[k^4(x)\int_{-b(x)/2}^{b(x)/2}\eta^2(x,y)dy - 2k^2(x)\right. \\ &\times\left.\int_{-b(x)/2}^{b(x)/2}\eta(x,y)\partial^2\eta(x,y)/\partial y^2 dy + \left[\beta/b(x)\right]^4\int_{-b(x)/2}^{b(x)/2}\eta^2(x,y)dy\right] \\ &- \omega^2\left[\rho_m h\int_{-b(x)/2}^{b(x)/2}\eta^2(x,y)dy + \rho_l\sum_{j=0}^{\infty}\frac{\left[\int_{-b(x)/2}^{b(x)/2}\eta(x,y)\cos\left(j\pi y/L_1\right)dy\right]^2}{\zeta_j\tanh\left(\zeta_j L_2\right)\int_{-L_1/2}^{L_1/2}\cos^2\left(j\pi y/L_1\right)dy}\right] \end{aligned} \tag{16}$$

Eq. (16) describes the dispersion relationship between $k(x)$ and $\omega$ at various $x$. The effect of surrounding fluid is found in the last term of Eq. (16). Since this term contributes to increase the effective mass for the vibration, the resonant frequency may be decreased by the surrounding fluid. From the average variation principle [14], it is known that the eikonal equation has the relationship with $W(x)$ as

$$W(x) = \frac{c}{\left(\dfrac{\partial f}{\partial k}\right)^{1/2}} \tag{17}$$

**Table 1**
Parameters for prediction.

| Parameter | Symbol | Value |
|---|---|---|
| Width of ABM (m) | $b(x)$ | $b(x) = 0.002 + 0.002x/L_3$ |
| Young's modulus of PVDF (Pa) | $E$ | $3 \times 10^9$[a] |
| Width of fluid channel (m) | $L_1$ | 0.017 |
| Depth of fluid channel (m) | $L_2$ | 0.004 |
| Length of ABM (m) | $L_3$ | 0.03 |
| Poisson ratio of PVDF | $\nu$ | 0.29[a] |
| Density of PVDF (kg/m$^3$) | $\rho_m$ | 1780 [15] |
| Density of silicone oil (kg/m$^3$) | $\rho_s$ | 873[b] |
| Density of air (kg/m$^3$) | $\rho_a$ | 1.2 [16] |

[a] From technical report by KUREHA.
[b] From technical report by Shin-Etsu Chemical.

where $c$ is a constant. Eq. (17) is the transport equation which describes the qualitative distribution of $W(x)$.

The parameters for the prediction are listed in Table 1. If the angular frequency $\omega$ is given as that of externally applied acoustic wave, only the wave number $k(x)$ is a variable to be solved in Eq. (16), where Eq. (16) is reduced to $f(k(x)) = 0$. At various $\omega$, Eq. (16) is solved numerically by the Newton method. The iteration procedure is repeated until the residual becomes less than a specified tolerance of $10^{-6}$. The term including summation is treated from $j = 0$ to 30, which is adequate for the tolerance. The calculation is conducted for the two cases of filling the fluid channel with the air and of that with the liquid. The frequency is changed in the ranges of 3.5–14.0 kHz in the air environment and 0.7–3.6 kHz in the liquid environment, respectively. At those frequencies, Eq. (16) gives solutions and $W(x)$ has a peak on ABM.

Fig. 3 shows $W(x)$ which describes the qualitative amplitude distribution defined by Eq. (17). $W(x)$ in the air environment of Fig. 3(a) shows a clear peak at each frequency, where the peak indicates the resonance at the local place. Comparing $W(x)$ at different frequencies, it is found that the peak position shifts to smaller $x$ as the frequency increases. It is also found that the peak value of $W(x)$ decreases as the frequency increases. Fig. 3(b) shows the $W(x)$ in the liquid environment. As same with the result in the air environment, the peak position shifts to smaller $x$ as the frequency increases. However, compared with the results in the air environment, $W(x)$ in the liquid environment shows peaks at smaller frequencies. By comparing the results at 3.5 kHz in Fig. 3(a) and (b), the effect of the surrounding fluid on $W(x)$ can be discussed in detail. Although ABM is vibrated at the same frequency, it is found that the peak position in the liquid environment is shifted to smaller $x$ and the form of $W(x)$ is moderated compared with those in the air environment. These results indicate that the stronger fluid-structure interaction due to the higher density decreases the resonant frequency and relaxes the resonance. Based on Eq. (16), the mechanism of decreasing the resonant frequency in the liquid environment is that the effective mass for the vibration is increased due to the much higher density of the liquid compared with that of the air. The reason for the moderated resonance is discussed later.

Fig. 4(a) shows the distributions of $k(x)$ in the air environment at 3.5, 6.0, 9.0, and 12.0 kHz. In Fig. 4(a), it is found that $k(x)$ in the air environment increases with $x$. There is a certain position of $x_{inc}$ where $k(x)$ rapidly increases. $x_{inc}$ is mathematically defined as the position where $k(x)$ gives the largest gradient. At larger $x$ than $x_{inc}$, $O(k(x))$ is $10^2$–$10^3$ m$^{-1}$ and the wavelength is 63–6.3 mm. At smaller $x$ than $x_{inc}$, $k(x)$ is very small which corresponds to the extremely long wavelength. Comparing the results at different frequencies, it is found that $x_{inc}$ becomes smaller at the higher frequency. It is also found that $x_{inc}$ is close to the peak position of $W(x)$ in Fig. 3(a). Since the result is obtained by the analysis based on the WKB solution, the wavelength should be short enough to treat $b(x)$ as a slowly varying function. Furthermore, $k(x)$ should be gradually changed by $x$. Thus, the precision of result should be relatively bad around $x_{inc}$ and at smaller $x$ than $x_{inc}$. Fig. 4(b) shows the $k(x)$ distributions in the liquid environment at 1.0, 2.0, 3.0, and 3.5 kHz. $k(x)$ in the liquid environment gradually increases with $x$ compared with that in the air environment. Although the resonant frequencies are different between in the air and in the liquid envi-

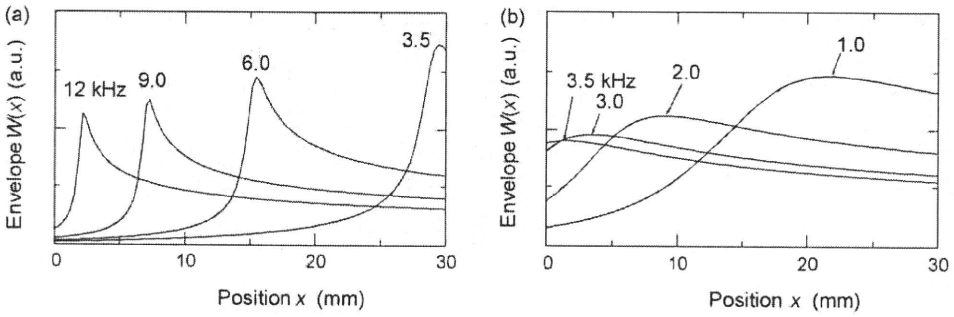


**Fig. 3.** Theoretical results of envelope function $W(x)$ in (a) air and in (b) liquid environments for various frequencies.

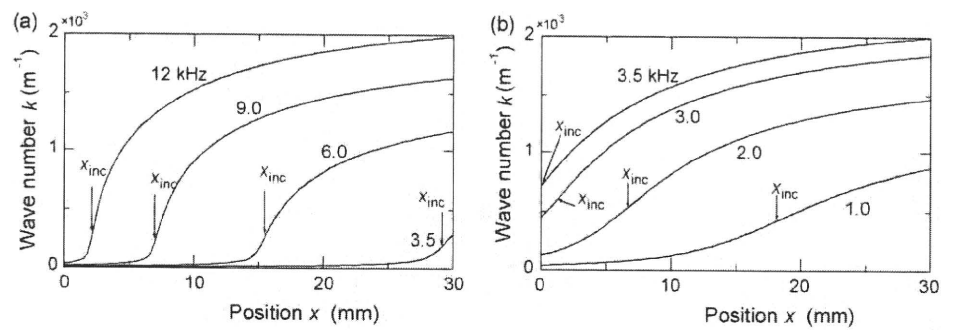


**Fig. 4.** Theoretical results of wave number $k(x)$ in (a) air and in (b) liquid environments for various frequencies.

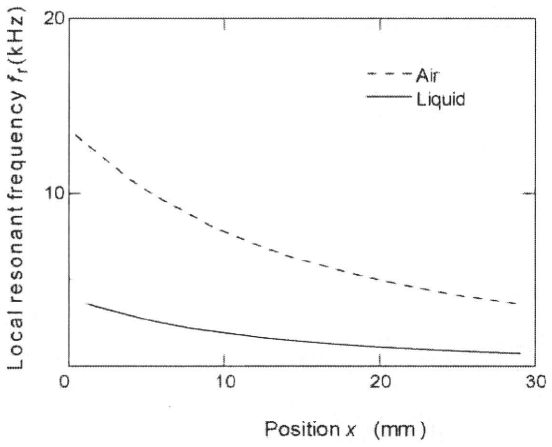


**Fig. 5.** Theoretical results of local resonant frequencies in air and in liquid environments.

ronments, the orders of $k(x)$ around $x_{inc}$ and at larger $x$ than $x_{inc}$ are similar to the results in the air environment. From this result, it can be said that the resonance is governed by the wavelength which is strongly related to the geometry of ABM. $x_{inc}$ is closely connected with the peak position of $W(x)$ shown in Fig. 3(b). Furthermore, the reason for the moderated resonance in the liquid environment can be explained by comparing Fig. 4(a) and (b). Since $k(x)$ in the air environment rapidly changes around the resonance place as shown in Fig. 4(a), the evolution of $W(x)$ also does. It is owing to the fact that the resonance condition is governed by the wavelength. On the contrary, since $k(x)$ in the liquid environment gradually changes around the resonance place as shown in Fig. 4(b), the peak of $W(x)$ becomes to be moderated.

Fig. 5 shows the relationship between the resonant frequency $f_r$ and $x$. Both $f_r$ in the air and in the liquid environments decrease as $x$ increases and $f_r$ in the liquid environment is lower than that in the air environment due to the increase of effective mass. Although the auditory frequency is widely ranged from $20 \times 10^{-3}$ to 20 kHz, the device can cover only the part of it. It works at the frequencies over the ranges of 3.5–14 kHz in the air environment and 0.7–3.6 kHz in the liquid environment, respectively. For the clinical application, the device should be optimized to realize the frequency selectivity in the required frequency range for a daily conversation. Furthermore, distribution of $f_r$ should be fitted to that in the biological system from the viewpoint of natural hearing. To solve these problems, the geometrical optimizations of ABM can be effectively carried out in our future work based on the theoretical analysis developed here.

The theoretical analysis is carried out based on the experimental condition, where only the bottom side of ABM faces to the liquid. In case of ABM facing to the liquid at both sides, the difference is found in the last term of Eq. (16) which includes the effect of surrounding fluid. In case of the same fluid channel is placed on the upper side of ABM and is filled with the same liquid, the last term is double of that in Eq. (16). Consequently, the larger effect of surrounding fluid is induced, that is, the further decrease of resonant frequency is found due to the increase of effective mass for the vibration, where the figure is omitted.

Furthermore, the theoretical analysis is carried out based on the assumption of the small amplitude. The basic equations are solved by WKB treatment which cannot quantitatively predict the vibrating amplitude. Therefore, it is difficult to precisely estimate the piezoelectric output which is determined by the strain in the membrane. The investigation on the piezoelectric output can be made by the numerical analysis based on the finite element method, which is our future research.

## 3. Results and discussion

### 3.1. Performance test in air environment

The basic vibrating characteristics of ABM in the air environment are investigated as a preliminary experiment. This experiment is conducted without filling the fluid channel with the silicone oil. The amplitude distributions of vibration are measured by applying acoustic waves of 75 dBSPL. The frequency is controlled over the range of 1.0–20.0 kHz, which covers the part of human's audible frequency. The amplitude of vibration becomes relatively small at the frequencies both lower than 3.0 kHz and higher than 18.0 kHz. It may be owing to that ABM is designed to have LRF for the first mode over the range of 3.5–14.0 kHz in the air environment. Fig. 6(a)–(d) show the amplitude distribution at $f$ = 4.0, 6.0, 9.0, and 12.0 kHz, respectively. The amplitude distribution clearly shows dependence on the frequency. The place with maximum amplitude, where ABM is locally resonating, shifts to the smaller $x$ as the frequency increases. This relationship between the position of resonating place and the frequency successfully has similarities with that of biological basilar membranes. Furthermore, in Fig. 6(c) and (d), it is found that there are several extrema indicated by arrows at the larger $x$ than that of resonating place. These may be induced by the standing wave due to the traveling waves to positive and negative directions of $x$. The reason why the standing wave is not observed at the smaller $x$ than that of resonating place is that the wavelength is relatively long at those positions. This is confirmed by the theoretical result of relatively small $k(x)$ as shown in Fig. 4(a). In the biological cochlea, the acoustic wave travels from the basal to the apex. However, in our experiment, it is applied to the entire ABM from the air. As a result, the relatively large effects of the standing waves are induced in our experiment due to the small damping effects from the surrounding fluid.

Fig. 7(a)–(c) show the frequency dependences of vibration and the piezoelectric output at Ch. 6, Ch. 12 and Ch. 18, respectively. The amplitudes of vibration and the piezoelectric output are plotted by a solid line and by a broken line, respectively. It seems that each electrode has a specific frequency where the electrode gives

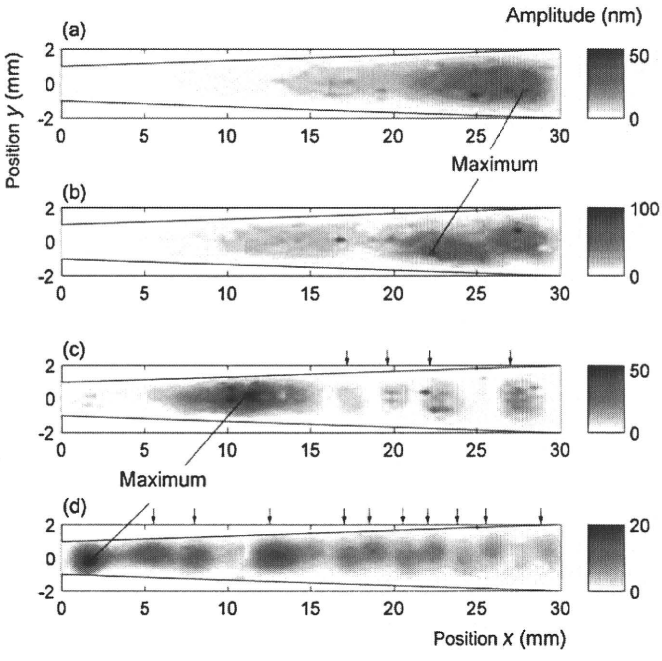


**Fig. 6.** Experimental results of contour maps of vibration amplitude at (a) $f$ = 4.0 kHz, (b) 6.0 kHz, (c) 9.0 kHz, and (d) 12.0 kHz in air.

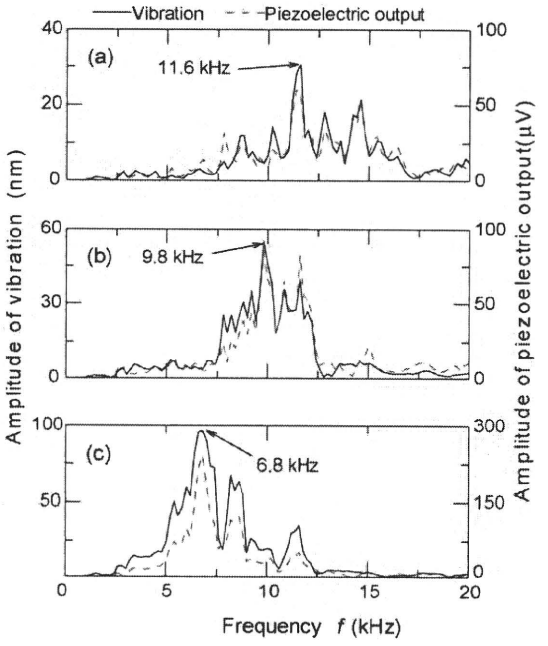


**Fig. 7.** Experimental results of vibration amplitude and piezoelectric output from (a) Ch. 6, (b) Ch. 12 and (c) Ch. 18 at various frequencies in air.

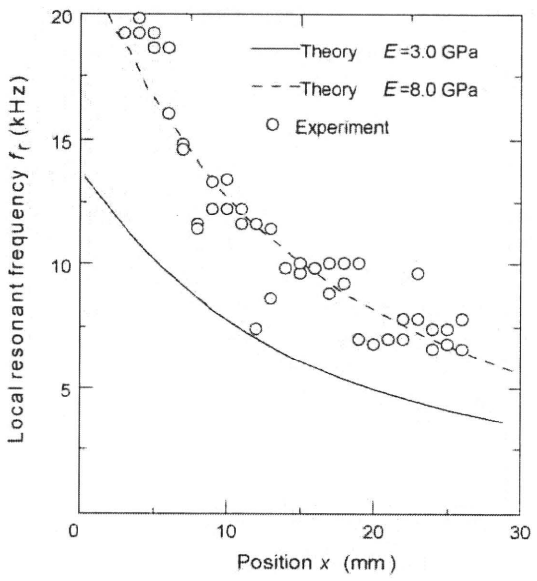


**Fig. 8.** Comparison of theoretically and experimentally obtained results of local resonant frequency $f_r$ in air.

relatively large outputs. The specific frequency is defined as LRF of electrode. LRF decreases as the channel number increases, i.e., as the position $x$ increases. Extremal amplitudes at other frequencies of LRF may indicate the effect of standing waves. That is, in case of the electrode locates on the antinode of standing wave, the amplitude from the electrode increases. On the other hand, in case of the electrode locates on the node, the amplitude decreases. As reported in Refs. [7,8,17], pretension in the membrane may be a main reason for the standing wave which results in the multiple-peaks as shown in Fig. 7. However, it is difficult to precisely control the pretension in our fabrication process. Therefore, the mechanism of this result remained to be solved in this study. The frequency dependences of vibration and the piezoelectric output are qualitatively similar to each other. The reason of their similarity can be explained as follows. Since ABM is relatively narrow in $y$ direction compared with that in the $x$ direction, the vibration is mainly effected by the boundary conditions at $y = \pm b(x)/2$. As the result of that, the piezoelectric output is dominated by the ABM's local structural strain in $y$ direction. Furthermore, the piezoelectric constant in $y$ direction is larger than that in $x$ direction. This may make the strong dependence of piezoelectric output on the strain in $y$ direction.

Fig. 8 shows the relationship between LRF $f_r$ and position $x$. Circles are LRF which are determined by the vibration and the piezoelectric output. LRF decreases from 19.8 to 6.6 kHz as $x$ increases. This experimental LRF is in qualitative agreement with the theoretical prediction of Eq. (16) which is drawn by the solid line. In the quantitative comparison, however, almost all experimental results are slightly higher than the predictions. One of possible reasons is the underestimation of $E$. Since $E$ from literatures widely distributes as 3.0–11.0 GPa [18,19], we used a reference value of 3.0 GPa for the prediction. If we use higher value of 8.0 GPa, the precision is improved as shown by the broken line in Fig. 8.

Fig. 9(a) shows the relationship between the external sound pressure and the amplitude of vibration in ABM. This investigation is conducted at LRF of each electrode. To show the results over the range of 60–90 dBSPL, those are drawn in the log-dBSPL plot. From the gradient of results, it is found that the amplitude of vibration at LRF linearly increases with the sound pressure. The amplitude increases with the channel number, that is, with ABM's width. Fig. 9(b) shows the relationship between the sound pressure and the amplitude of piezoelectric output. The amplitude of piezoelectric output also shows the linear relationship with the sound pressure. These results suggest that the device can detect not only the frequency of acoustic wave but also the magnitude of it.

### 3.2. Performance test in liquid environment

The performance of device in the liquid environment is investigated by filling the fluid channel with the silicone oil with the

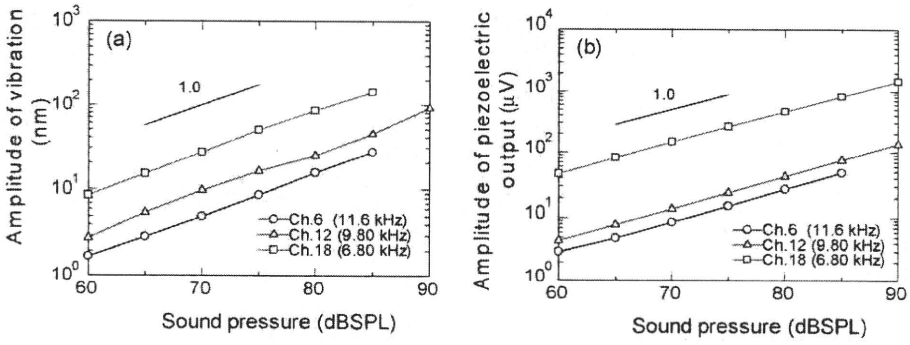


**Fig. 9.** Experimental results in effect of sound pressure on amplitudes (a) of vibration and (b) of piezoelectric output in air.

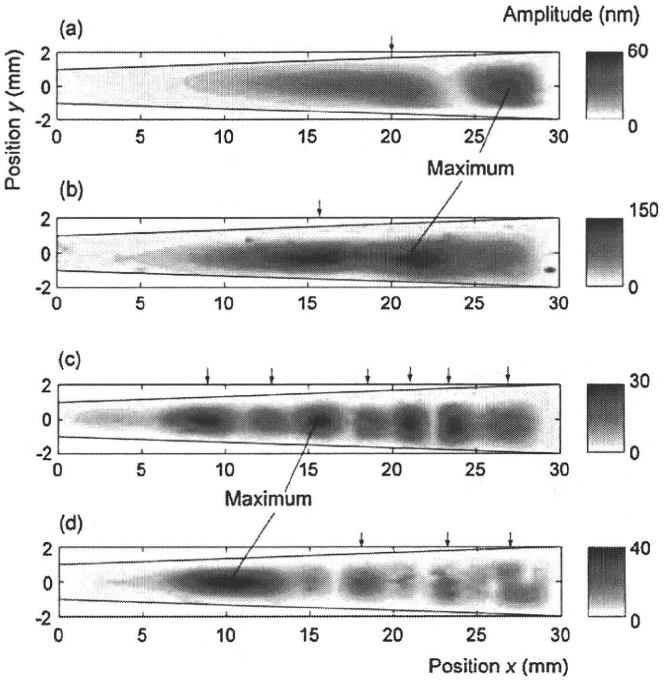


**Fig. 10.** Experimental results of contour maps of vibration amplitude at (a) $f$ = 1.5 kHz, (b) 2.0 kHz, (c) 3.0 kHz and (d) 4.0 kHz in silicone oil of 1.75 × $10^{-3}$ Pa s.

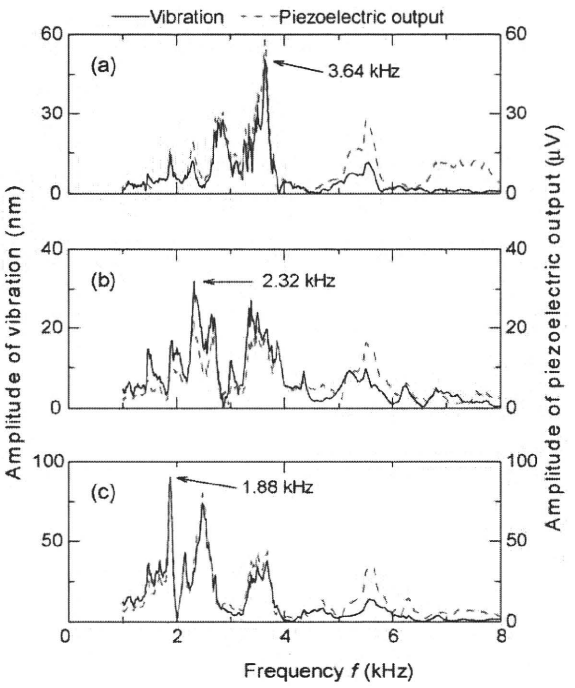


**Fig. 11.** Experimental results of vibration amplitude and piezoelectric output from (a) Ch. 6, (b) Ch. 12 and (c) Ch. 18 at various frequencies in silicone oil of 1.75 × $10^{-3}$ Pa s.

viscosity of 1.75 × $10^{-3}$ Pa s. This investigation is intended to test the applicability of device for implanting into the cochlea. Since the outputs from ABM are relatively small compared with that in the air environment, the sound pressure is increased to be 85 dBSPL for this experiment. This decrease of outputs in the silicone oil may be caused by energy dissipation in liquid environment due to the viscosity and the stronger fluid-structure interaction of ABM due to the density, however, the detailed mechanism has not been clarified. Fig. 10 shows the contour maps of amplitude distribution at (a)$f$ = 1.5 kHz, (b)2.0 kHz, (c)3.0 kHz and (d) 4.0 kHz, respectively. The qualitative frequency dependence of vibration is similar to that in the air environment. That is, the location with the maximum amplitude is shifted to the smaller $x$ as the frequency increases. However, the frequency ranges where ABM shows peak amplitude in the silicone oil are lower than that in the air environment. Comparing Fig. 6(a) and Fig. 10(d), the effect of surrounding fluid can be discussed in detail. In spite of driving the device at the same frequency of 4.0 kHz, these results clearly show the different vibration behavior. It is found that the maximum amplitude is found at the smaller $x$ in the silicone oil compared with that in the air environment. This difference may be caused by the fluid-structure interaction as discussed in the earlier section. That is, compared with the result in the air environment, the effective mass for the vibration is increased in the silicone oil. As a result, the place with maximum amplitude is shifted to the smaller $x$ in the silicone oil at the same frequency. Furthermore, the effects of standing wave in the silicone oil which are indicated by arrows seem relatively large compared with that in the air environment. This fact is predicted by the theoretical analysis that the resonance is relaxed due to the surrounding liquid as shown in Fig. 3.

Fig. 11 shows the frequency dependences of vibration and piezoelectric output, where they are indicated by a solid line and the broken one, respectively. As same with those in the air environment, the two amplitudes show the similar tendency to each other. The amplitudes have peaks at each specific frequency which is also described as LRF for convenience. LRF of Ch. 6, Ch. 12, and Ch. 18 are obtained as 3.64, 2.32, and 1.88 kHz, respectively. From Fig. 11, it is confirmed that the ABM's frequency selectivity is successfully realized even in the liquid environment. However, comparing Figs. 7 and 11, the peak height at the LRF becomes low, i.e., the selectivity seems worse than that in the air environment. This result qualitatively agrees with the theoretical result that the peak is relaxed in the liquid environment as shown in Fig. 3. In order to dramatically improve the frequency selectivity, it is expected that the sensor including the active feedback control which mimics the biological cochlea should be developed in future.

Fig. 12 shows the relationship between $f_r$ and $x$ in the silicone oil. From Fig. 12, it is found that the LRF decreases from 4.9 to 1.4 kHz as $x$ increases, where the range is lower than that in the air environment. The experimentally obtained LRF is compared

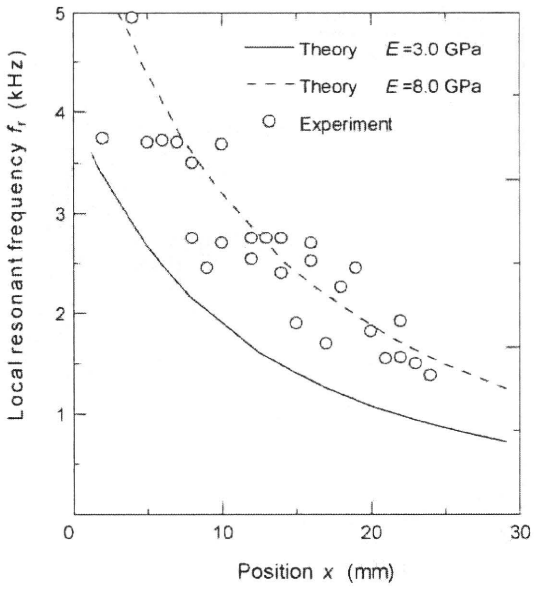


**Fig. 12.** Comparison of theoretically and experimentally obtained results of local resonant frequency $f_r$ in silicon oil of 1.75 × $10^{-3}$ Pa s.

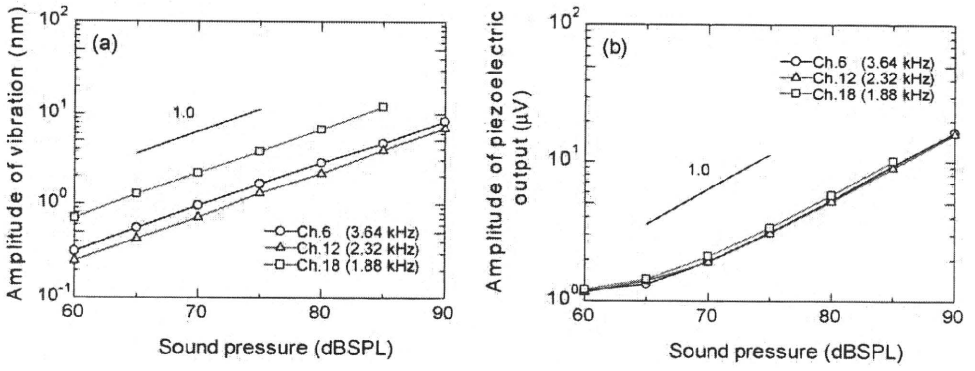


**Fig. 13.** Experimental results in effect of sound pressure on amplitudes (a) of vibration and (b) of piezoelectric output in silicone oil of $1.75 \times 10^{-3}$ Pa s.

with the theoretically obtained one in Fig. 12. The predicted LRF of $E = 8.0$ GPa which is drawn by the broken line reasonably agrees with the experimentally obtained ones. From this agreement, it can be said that the theoretical analysis well reproduces the effect of the fluid-structure interaction on LRF. Since the theoretical analysis is carried out with inviscid fluid model, it can also be said that the decrease of LRF in the liquid environment is governed by the increase of effective mass for the vibration under the condition of constant sound pressure.

Fig. 13(a) shows the relationships between the sound pressure and the amplitudes of vibration. The amplitude of vibration linearly increases with the sound pressure. However, the amplitude of piezoelectric output shown in Fig. 13 (b) seems to be nonlinear especially at the low sound pressure level of 60–70 dBSPL. It may be due to the viscosity of liquid, however, it is difficult to confirm the reason for the nonlinear relationship due to the lack of the basic knowledge, where it is in our future work. As shown in Fig. 13(b), the amplitude of piezoelectric output is about 16 μV at 90 dBSPL in the silicone oil. The acoustic wave of 90 dBSPL is relatively loud for the normal hearing. Even applying such a high sound pressure, the developed device can generate several tens of μV at most. To effectively stimulate nerve cells [20], the electric output should be amplified. One of the methods for the amplification is to use equipment such as a hearing aid, where it amplifies the sound pressure. Another solution is the downsizing of device using a fully micromachining process, since the thinner membrane can generate the larger voltage. That is, the piezoelectric voltage $V_p$ is proportional to the stress $\sigma$ and the square of thickness $h$ as $V_p \propto \sigma h^2$. On the other hand, the stress $\sigma$ of ABM is inversely proportional to the cube of thickness as $\sigma \propto h^{-3}$. Consequently, the voltage is inversely proportional to the thickness as $V_p \propto h^{-1}$. The reduction of thickness can be easily realized by means of microfabrication and the thin films technologies. Thus, the implantable device will be developed based on those technologies in our future work.

### 3.3. *Effect of viscosity on frequency selectivity*

Fig. 14 shows the contour maps of amplitude distribution using the higher viscous silicone oil of $1.75 \times 10^{-2}$ Pa s at (a)$f = 1.5$ kHz, (b)2.0 kHz, (c)3.0 kHz and (d) 4.0 kHz, respectively. The viscosity of the silicone oil is ten times higher than that in the previous section. The positions of maximum amplitude are $x = 28.0$, 24.0, 20.5, and 10.5 mm for $f = 1.5$, 2.0, 3.0, and 4.0 kHz, respectively as shown in Fig. 14. On the other hand, those are $x = 27.0$, 21.0, 16.0, and 10.0 mm in the results of $1.75 \times 10^{-3}$ Pa s as shown in Fig. 10. From this result, it can be said that the effect of viscosity on the position of the resonating place seems small. It is also found that the local maximum amplitudes due to the standing wave are relatively small in Fig. 14 compared with those in Fig. 10. That is

**Table 2**
Ratio $a_1/a_2$ of height between the highest peak and the secondary highest one.

| Frequency $f$ (Hz) | Ratio at $1.75 \times 10^{-3}$ Pa s $a_1/a_2$ | Ratio at $1.75 \times 10^{-2}$ Pa s $a_1/a_2$ |
|---|---|---|
| 1.5 | 1.52 | 1.69 |
| 2.0 | 1.03 | 1.56 |
| 3.0 | 1.08 | 1.96 |
| 4.0 | 1.89 | 2.08 |

quantitatively confirmed by the ratio $a_1/a_2$ which is the ratio of amplitudes between the highest peak $a_1$ and the secondary highest peak $a_2$ in Table 2. Comparing the results between $1.75 \times 10^{-3}$ Pa s and $1.75 \times 10^{-2}$ Pa s, it is found that the highest peak is significant in the higher viscous silicone oil. This may be caused because the wave is damped more rapidly in the higher viscous one. From the viewpoint of application, this result indicates that the effect of viscosity may contribute to improve the frequency selectivity. It is also possible to discuss the effect of viscosity by comparing the result between in the air and in the liquid environments. However, there are two different types of fluid-structure interactions of the increase in the effective mass and the viscous damping between

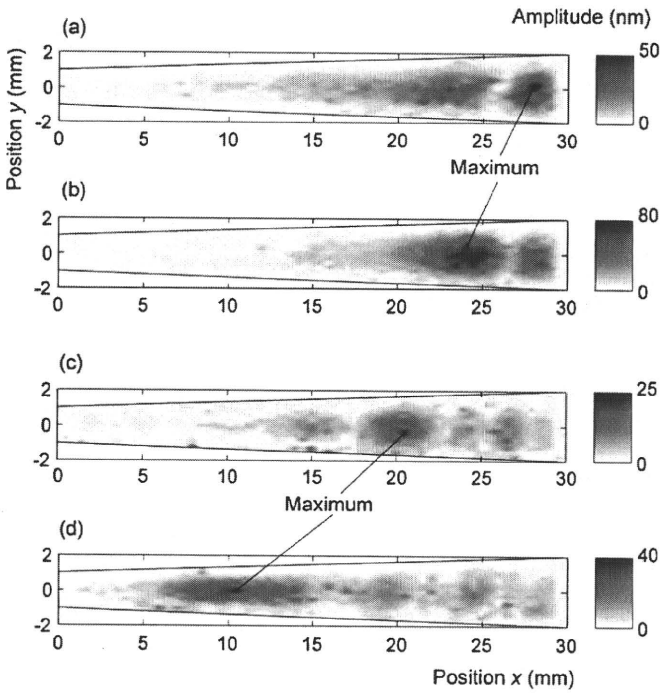


**Fig. 14.** Experimental results of contour maps of vibration amplitude at (a) $f = 1.5$ kHz, (b) 2.0 kHz, (c) 3.0 kHz and (d) 4.0 kHz in silicone oil of $1.75 \times 10^{-2}$ Pa s.

those conditions. Since they contribute to the frequency selectivity oppositely, it is difficult to discuss separately. The development of theoretical analysis using full Navier-Stokes equation should be made in future research.

## 4. Concluding remarks

In this paper, we reported a novel piezoelectric artificial cochlea which worked as a sensor with the acoustic/electric conversion and with the frequency selectivity based on MEMS technology. The basic performances of prototype device both in the air and in the liquid environments were investigated experimentally and theoretically.

The vibrating characteristics of trapezoidal ABM were measured by applying acoustic waves at a certain frequency. The location with the maximum amplitude was shifted toward narrower area of trapezoidal ABM as the frequency increased. This phenomenon indicated that the developed device successfully realized the frequency selectivity.

The frequency dependences of vibration and piezoelectric output were investigated both in the air and in the silicone oil of $1.75 \times 10^{-3}$ Pa s. The resonant frequencies were determined to be over the ranges of 6.6–19.8 kHz in the air and 1.4–4.9 kHz in the silicone oil, respectively. The decrease in the resonant frequency due to the silicone oil must be the effect of fluid-structure interaction, that is, the interaction between the acoustic wave in the fluid and the membrane vibration. The interaction contributed to increase the effective mass for the vibration. This consideration was confirmed by the reasonable agreement between the experiment and the theory in terms of local resonant frequency.

The viscous effect of surrounding fluid on the vibration was explored using the higher viscous silicone oil of $1.75 \times 10^{-2}$ Pa s. The effect on the resonating place seemed to be small between $1.75 \times 10^{-3}$ and $1.75 \times 10^{-2}$ Pa s. However, it was found that the higher viscous liquid suppressed the standing wave and improved the frequency selectivity.

To develop the fully implantable device in our future work, the amplification of voltage may be required to effectively stimulate nerve cells. Furthermore, the present device is relatively large for the implantation into a cochlea. These problems can be solved by the use of microfabrication and thin films technologies. The miniaturization is accomplished by the technology straightforward. And the larger electric signals can be generated using the thinner ABM, since the voltage is expected to be inversed proportional to the thickness. As a matter of course, these further developments must be conducted considering the frequency dependence. Thus, the theoretical approach which is described here is useful to design it in our future work.

## References

[1] F.G. Zeng, Trends in cochlear implants, Trends Amplification 8 (1) (2004) T1–T34.
[2] S.B. Waltzman, Cochlear implants: current status, Expert Rev. Med. Dev. 3 (5) (2006) 647–655.
[3] G.V. Békésy, Current status of theories of hearing, Science 123 (3201) (1956) 779–783.
[4] G.V. Békésy, Hearing theories and complex sounds, J. Acoust. Soc. Am. 35 (4) (1963) 588–601.
[5] K. Tanaka, M. Abe, S. Ando, A novel mechanical cochlea "fishbone" with dual sensor/actuator characteristics, IEEE ASME Trans. Mechatron. 3 (2) (1998) 98–105.
[6] T. Xu, M. Bachman, F.G. Zeng, G.P. Li, Polymeric micro-cantilever array for auditory front-end processing, Sens. Actuators A Phys. 114 (2–3) (2004) 176–182.
[7] F. Chen, H.I. Cohen, T.G. Bifano, J. Castle, J. Fortin, C. Kapusta, D.C. Mountain, A. Zosuls, A.E. Hubbard, A hydromechanical biomimetic cochlea: experiments and models, J. Acoust. Soc. Am. 119 (1) (2006) 394–405.
[8] R.D. White, K. Grosh, Microengineered hydromechanical cochlear model, Proc. Natl. Acad. Sci. U.S.A. 102 (5) (2005) 1296–1301.
[9] M.J. Wittbrodt, C.R. Steele, S. Puria, Developing a physical model of the human cochlea using microfabrication methods, Audiol. Neurootol. 11 (2) (2006) 104–112.
[10] C.R. Steele, L.A. Taber, Comparison of WKB calculations and experimental results for three-dimensional cochlear models, J. Acoust. Soc. Am. 65 (4) (1979) 1007–1018.
[11] J.D. Bronzino, The Biomedical Engineering Handbook, CRC Press, 1995.
[12] G. Zhou, L. Bintz, D.Z. Anderson, A life-sized physical model of the human cochlea with optical holographic readout, J. Acoust. Soc. Am. 93 (3) (1993) 1516–1523.
[13] J.H. ten Kate, J.W. Kuiper, The viscosity of the pike's endolymph, J. Exp. Biol. 53 (2) (1970) 495–500.
[14] G.B. Whitham, Linear and Nonlinear Waves, Wiley-Interscience, 1974.
[15] M. Chanda, S.K. Roy, Plastic Technology Handbook, CRC press, 2006, pp. 5–52.
[16] National Astronomical Observatory of Japan, Chronological scientific tables (2009), Maruzen.
[17] K.M. Lim, A.M. Fitzgerald, C.R. Steele, Building a physical cochlear model on a silicon chip, in: H. Wada, T. Takasaka, K. Ikeda, K. Ohyama, T. Koike (Eds.), Recent Developments in Auditory Mechanics, World scientific, 1999, pp. 223–229.
[18] J. Sirohi, I. Chopra, Fundamental understanding of piezoelectric strain sensors, J. Intell. Mater. Syst. Struct. 11 (4) (2000) 246–257.
[19] H. Ohigashi, Electromechanical properties of polarized polyvinylidene fluoride films as studied by the piezoelectric resonance method, J. Appl. Phys. 47 (3) (1976) 949–955.
[20] Y. Jimbo, T. Tateno, H.P.C. Robinson, Simultaneous induction of pathway-specific potentiation and depression in networks of cortical neurons, Biophys. J. 76 (2) (1999) 670–678.

## Biographies

**Hirofumi Shintaku** received B.S., M.S., and Ph.D. degrees from Department of Mechanical Engineering, Kyoto University, Japan, in 2002, 2004, and 2006, respectively. Since 2006, he has been an Assistant Professor in Department of Mechanical Science and Bioengineering, Graduate School of Engineering Science, Osaka University, Japan. His current research area is fluid dynamics in the micro and nano meter scales.

**Takayuki Nakagawa** received M.D. and Ph.D. from Medical School, Osaka City University, Japan in 1989 and 1995, respectively. From 1995 to 2001, he was a Department Director in Department of Otolaryngology, Yodogawa Christian's Hospital, Osaka, Japan. From 2001 to 2008, he was an Assistant Professor in Department of Medicine, Graduate School of Medicine, Kyoto University, Japan. Since 2008, he has been a Lecturer in Kyoto University.

**Dai Kitagawa** received B.S. degree from Department of Mechanical Science and Bioengineering, Osaka University, Japan, in 2007. Since 2007, he has been a master course student in Department of Mechanical Science and Bioengineering, Graduate School of Engineering Science, Osaka University.

**Harto Tanujaya** received B.S. and M.S. degree from Tarumanagara University, Indonesia and University of Indonesia in 1996 and 1999, respectively. Since 2000, he has been a Lecturer at Department of Mechanical Engineering, Faculty of Engineering, Tarumanagara University. Furthermore, since 2007, he has been a Ph.D. course student in the Department of Mechanical Science and Bioengineering, Graduate School of Engineering Science, Osaka University, Japan.

**Satoyuki Kawano** received B.S., M.S., and Ph.D. degrees in Mechanical Engineering from Tohoku University, Japan in 1987, 1989 and 1992, respectively. Following graduation he was a Postdoctoral Fellow of the Japan Society for the Promotion of Science in 1992. He was appointed as a Research Assistant in 1993 and as an Associate Professor in 1996 at Tohoku University. In the year of 2005, he was appointed as a Professor at Osaka University where he served as the Chair of the Division of Mechanical Engineering of the Graduate School of Engineering Science from 2006 to 2009. His current research interest is molecular fluid dynamics including interfacial phenomena, plasmas, blood cells and biomacromolecules.

**Juichi Ito** received M.D. and Ph.D. from Department of Medicine, Kyoto University, Japan, in 1975 and 1983, respectively. From 1983 to 1985, he was an Assistant Professor in Neurology, University of California, Los Angeles. From 1985 to 1990, he was a Lecturer in Department of Otolaryngology Head and Neck Surgery Kyoto University Hospital. From 1990 to 2000, he was a Chief in Otorhinolaryngology and Broncho-Esophagology, Otsu Red-Cross Hospital. Since 2000, he has been a Professor and Chairman of Department of Otolaryngology Head and Neck Surgery, Graduate School of Medicine, Kyoto University.

Journal of Biomechanical Science and Engineering

Vol. 5, No. 3, 2010

# Culturing Neurons on MEMS Fabricated P(VDF-TrFE) Films for Implantable Artificial Cochlea*

Hirofumi SHINTAKU**, Takashi TATENO**, Nobuyoshi TSUCHIOKA**, Harto TANUJAYA**, Takayuki NAKAGAWA***, Juichi ITO*** and Satoyuki KAWANO**

**Department of Mechanical Science and Bioengineering, Graduate School of Engineering Science, Osaka University, Machikaneyama-cho 1-3, Toyonaka, Osaka 560-8531, Japan
E-mail: shintaku@me.es.osaka-u.ac.jp

***Department of Otolaryngology, Head and Neck Surgery, Graduate School of Medicine, Kyoto University, Kawahara-cho 54,Shogoin, Sakyo-ku, Kyoto 606-8507, Japan

**Abstract**

In this paper, we report an *in vitro* study on the biocompatibility of poly(vinylidene fluoride-trifluoroethylene) (P(VDF-TrFE)) films for the implantable artificial cochlea. The implantable artificial cochlea comprises a piezoelectric membrane made of P(VDF-TrFE), platinum (Pt) thin film electrodes, and a silicon substrate which are designed to stimulate neurons in a cochlea and fabricated by microelectromechanical systems (MEMS) and thin film technologies. The biocompatibility of P(VDF-TrFE) film is evaluated by culturing cerebral cortical neurons from rats on it. The fibronectin from human plasma and the collagen from the calf skin are used as the cell adhesion factors. Since neurons extend dendrites and axons from the somata, it is found that the neurons are successfully cultured on the surface of P(VDF-TrFE) films modified both by the fibronectin and by the collagen. Furthermore, it is also found that the neurons are also successfully cultured over the Pt electrode on the P(VDF-TrFE) of the implantable artificial cochlea modified by the fibronectin. Consequently, the biocompatibility and the applicability of the MEMS fabricated P(VDF-TrFE) films and the implantable artificial cochlea are confirmed.

***Key words***: Biocompatibility, MEMS, Cerebral Cortical Neuron, Medical Equipment, Biomechanical Engineering, Piezoelectric Device

## 1. Introduction

Piezoelectric materials are promising ones in the field of implantable artificial organs, since they can be used for electric power generators and sensors using the direct piezoelectric effect and for actuators using the inverse piezoelectric effect. For instance, Lewandowski et al.[1] proposed a piezoelectric power generator with a muscle-tendon unit. Platt et al.[2] proposed a self-powered embedded sensor for orthopedic implants. Schubert et al.[3] and Schrag et al.[4] proposed micropumps using piezoelectric actuators for an implantable artificial pancreas and artificial bowel sphincter, respectively. Furthermore, authors have proposed a piezoelectric artificial cochlea which realizes the acoustic/electric conversion and the frequency selectivity without an externally supplying energy[5]-[7].

Figure 1 shows a schematic of implantable artificial cochlea we have proposed. The

*Received 13 June, 2009 (No. 09-0262)
[DOI: 10.1299/jbse.5.229]

device comprises a piezoelectric membrane (ABM) made of poly(vinylidene fluoride-trifluoroethylene) (P(VDF-TrFE)) and discrete electrodes made of platinum (Pt) thin films, which are fabricated on a silicon (Si) substrate by microelectromechannical systems (MEMS) and thin film technologies. When the curved ABM is extended straight, it can be seen that ABM has a trapezoidal shape. The shape which is designed to mimic the biological system, i.e. the basilar membrane in cochlea, enables to analyze the frequency of acoustic wave. To cure the sensorineural hearing loss in the future, the implantable artificial cochlea is inserted into a cochlea which is filled with lymph fluid. ABM in the cochlea is vibrated by externally applying acoustic waves which is transmitted through the outer ear and the middle one. The mechanical deformation of ABM due to the vibration is converted to electric signals by the piezoelectric effect of P(VDF-TrFE) and the electric signals stimulate neurons in the cochlea. Since the proposed device is basically developed by microfabrication technologies, the electrodes can be easily integrated and their number can be increased, whereas the conventional system is limited by the relatively small number of electrodes as 12-22[8]-[10]. Furthermore, since the frequency of acoustic wave is analyzed by a biomimetic system, the device may realize more "natural hearing" compared with the conventional system.

The basic mechanisms of frequency analysis and acoustic/electric conversion have been studied using a prototype device fabricated by bulk processes[5],[6]. The effects of surrounding fluid of ABM have been studied by the comparison between theoretical results and experimental ones[6]. Furthermore, for the miniaturization of device and the amplification of electric signals, a fabrication process based on MEMS and thin film technologies have been developed[7]. Although the ultimate goal of our studies is to develop the fully self-contained implantable artificial cochlea, the biocompatibility of device has not been discussed. Since Si and Pt are relatively popular materials in the MEMS field, there are literatures that discuss their biocompatibility[11]. However, as far as authors are aware, there are few papers that evaluate the biocompatibility of P(VDF-TrFE) films fabricated by MEMS processes.

Thus, in this paper, we investigate the biocompatibility of P(VDF-TrFE) films for the proposed artificial cochlea in terms of cytotoxicity. To transfer the electric signal from Pt electrodes to auditory neurons in the cochlea over the P(VDF-TrFE) thin film, the neurons should be cultured or at least they should extend neurites on P(VDF-TrFE) films. Therefore, the *in vitro* experiment is carried out by culturing cerebral cortical neurons from rats on the P(VDF-TrFE) films. The cultured neurons are labeled by the fluorescent Nissl stain and observed by a fluorescent microscope. To observe the detailed configurations of neurons by the phase contrast microscope, P(VDF-TrFE) films are also fabricated on glass substrates, instead of Si substrates. Since MEMS fabricated P(VDF-TrFE) films can be applied to develop other biomedical devices, the results obtained here provide not only the fundamental knowledge on the biocompatibility of proposed artificial cochlea but also on that of P(VDF-TrFE) films for other artificial organs.

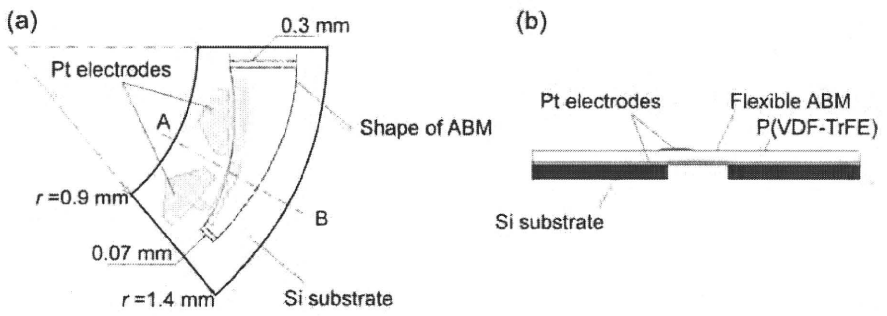


Fig. 1 Schematic of fully self-contained implantable artificial cochlea[7]: (a) top view and (b) cross sectional view at AB of (a).

## 2. Materials and methods

The fabrication process of implantable artificial cochlea is described as follows. The surface of Si substrate (100) is pretreated by hexamethyldisilazane (OAP, Tokyo Ohka Kogyo) to enhance the adhesion of P(VDF-TrFE) film. Then, a N,N-dimethylformamide (DMF) solution including P(VDF-TrFE) (KF-W#2200 P(VDF-TrFE), KUREHA) at the concentration of 8.0 wt% is spun on the substrate. The substrate is heated on a hotplate at 50 °C for 12 hours to evaporate DMF and at 145 °C for 2 hours to crystallize P(VDF-TrFE). The Pt electrodes are fabricated on the P(VDF-TrFE) film using a lift off process. The etching process of Si which makes the P(VDF-TrFE) film to be a flexible ABM is omitted in this study, since that is not necessary to discuss the biocompatibility. For the purpose of optical observation using a phase contrast microscope, glass substrates (Micro slide glass, Matsunami) are also used to fabricate P(VDF-TrFE) films instead of Si substrates.

A piece of processed substrate is sterilized by spraying with 70 % ethanol and is put into tissue culture dishes made of polystyrene. Then, the surfaces of substrates are modified by cell adhesion factors. Since it is obvious that the adherent cells have difficulties in growing on the hydrophobic surfaces such as P(VDF-TrFE), two types of popular cell adhesion factors, the fibronectin from the human plasma[12] and the collagen from the calf skin[13], are used to focus the discussion on the cytotoxicity of the material. The process of surface modification is briefly described as follows. For the modification by fibronectin, the substrate is immersed in phosphate buffered saline (PBS) containing fibronectin (F0895, Sigma Aldrich Japan) at the concentration of $6.7\times10^{-3}$ g/ml and is incubated at room temperature for more than 45 min. After that, the residual solution is removed. On the other hand, for the modification by the collagen, the substrate is immersed in 0.1 M acetic acid containing 0.1 wt% collagen (C8919, Sigma Aldrich Japan) and is incubated at 4 °C for 12 hours. After removing the residual solution, the substrate is kept at room temperature to be dried for 12 hours.

Dulbecco's modified Eagle's medium (DMEM, Gibco) which contains fetal bovine serum of 5.0 vol%, horse serum of 5.0 vol%, penicillin of $6.2\times10^{-4}$ g/ml, and insulin of $3.5\times10^{-5}$ g/ml[14] is poured into the tissue culture dish which contains the surface modified substrate. Then, the DMEM containing dissociated cerebral cortical neurons from rats at postnatal day 1 is introduced to the dish. Since it is quite difficult to obtain enough amounts of neurons from a cochlea, cerebral cortical neurons are used. However, the results are applicable to discuss the biocompatibility as a first step. The dish is placed in an incubator which is maintained at 37 °C and 5% $CO_2$ to culture neurons on the substrates for 3 days. After culturing 3 days, the neuron is fixed by 4% paraformaldehyde and labeled by fluorescent Nissl stains (NeuroTrace™ 500/525 green, Sigma Aldrich Japan)[15] for the subsequent optical observation. Since the Nissl substance labeled by the stain is abundant in neurons, cells with high fluorescent intensity indicate neurons. The viability is evaluated based on the morphology of cells observed by the fluorescent microscope and the phase contrast one. Although most of cells used here are neurons, cells include some glia ones. Thus, the neurons are distinguished based on the observations using both fluorescent photographs and phase contrast ones.

## 3. Results and discussion

Figures 2 (a), (b), and (c) show a phase contrast photograph, a fluorescent one, and a merged one of Figs. 2(a) and 2(b), respectively, observed at a same place of P(VDF-TrFE) fabricated on the glass substrate and modified by the fibronectin. Since the P(VDF-TrFE) and the glass substrate are transparent, it is possible to observe neurons, dendrites, and axons using a phase contrast microscope as shown in Fig. 2(a). Symbols of Ss and Ds in Fig. 2(a) are considered as somata and dendrites which adhere on the substrate, respectively,

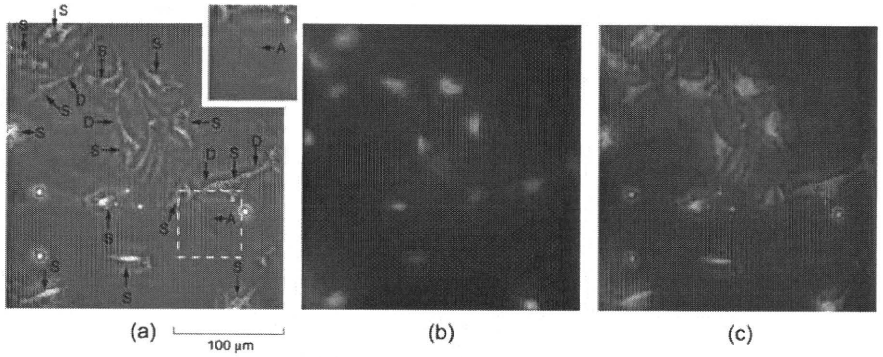


Fig. 2 (a) Phase contrast photograph, (b) fluorescent one, and (c) merged one of (a) and (b) of cultured neurons over P(VDF-TrFE) film modified by fibronectin and fabricated on glass substrate. Symbols A, D, and S indicate axon, dendrite, and soma, respectively. Inset in (a) is enlarged view around axon of A.

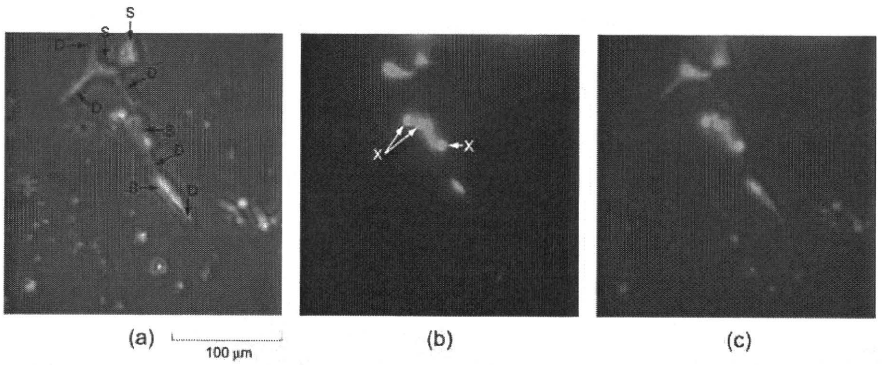


Fig. 3 (a) Phase contrast photograph, (b) fluorescent one, and (c) merged one of (a) and (b) of cultured neurons over P(VDF-TrFE) film modified by collagen and fabricated on glass substrate. Symbols D, S, and X indicate dendrite, soma, and dead cell, respectively.

since the stained areas in Fig. 2(b) correspond to the place of somata and dendrites as shown in Fig. 2(c). Furthermore, symbol A in the inset of Fig. 2(a) must be an axon. From these observation, it can be said that the neurons are successfully cultured on the P(VDF-TrFE) film modified by the fibronectin.

Figures 3 (a), (b), and (c) show a phase contrast photograph, a fluorescent one, and a merged one of Figs. 3(a) and 3(b), respectively, observed at a same place of P(VDF-TrFE) fabricated on the glass substrate and modified by the collagen. Symbols of Ss and Ds in Fig. 3(a) indicate somata and dendrites, respectively, where it is confirmed by the fluorescent photograph of Fig. 3(b) and by the merged one of Fig. 3(c). From the fluorescent photograph of Fig. 3(b), it is possible to roughly evaluate the viability of neurons based on the shapes of stained areas, where living and dead neurons seem to be distorted shapes and circular shapes, respectively. Xs in Fig.3 (b) must be dead neurons which are approximately circular shape. However, since most neurons are living and extend dendrites, it can be said that neurons are successfully cultured on the P(VDF-TrFE) film modified by the collagen. As shown in Figs. 2 and 3, the qualitative difference in terms of viability of neurons is not found between the cell adhesion factors of the fibronectin and the collagen. Consequently, it is found that P(VDF-TrFE) is applicable to a biocompatible material in terms of culturing neurons on it.

Figure 4 shows fluorescent photographs of cultured neurons over the P(VDF-TrFE) film fabricated on a Si substrate and modified by the fibronectin, that is, our proposed implantable artificial cochlea. The relatively dark background at the right half of Fig. 4 (a) indicates the Pt electrode on the P(VDF-TrFE) film. Since the Si substrate is not transparent, the evaluation on the cell viability is carried out based on this fluorescent

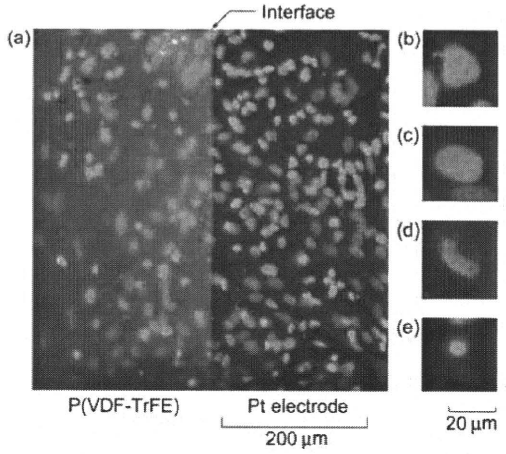


Fig. 4 (a) Fluorescent photograph of cultured neurons over P(VDF-TrFE) film and Pt electrode modified by fibronectin on Si substrate; (b)~(d) distorted stained area corresponding to living neurons and (e) circular area corresponding to dead one.

photograph. Although it is relatively difficult to strictly distinguish between the neuron and the glia cell only from Fig.4 (a), it is found that there are many stained areas with distorted shape. These distorted stained areas correspond to the living neurons or glia cells which adhere on the surface of substrate, where typical distorted and stained areas are shown in Fig.4 (b)~(d). In contrast, the dead cells should have a circular shape as shown in Fig.4 (e), because they do not adhere on the surface of materials. It is found that there are few dead cells in Fig. 4(a). In terms of cell viability, there is no qualitative difference between the area of the P(VDF-TrFE) and the Pt electrode. It may be because the surfaces are uniformly modified by the fibronectin. Furthermore, it is confirmed that there are living neurons or glia cells on the interface between P(VDF-TrFE) and the electrode. From these result, it can be concluded that the Pt thin film electrode is biocompatible and the electrodes must work well for stimulating neurons on it. Consequently, the biocompatibility of proposed artificial cochlea is also confirmed in cytotoxicity. In addition, it is important to discuss the *in vivo* biocompatibility in the context of sensitization, irritation, chronic toxicity, genotoxicity, and fibrous encapsulation.

The present study provides the fundamental knowledge on the biocompatibility of MEMS fabricated P(VDF-TrFE) films and proposed artificial cochlea. However, from the viewpoint of ABM's vibrating characteristics, the neurons should not be cultured on the flexible ABM as shown in Fig. 1(b), since the eigen frequency of vibration is designed before the implantation into a cochlea[7], where the effect of neurons on the vibration is not considered. On the contrary, the neurons should be cultured on the electrodes to be stimulated effectively. Thus, the area where neurons are cultured should be controlled by patterning the cell adhesion factor using MEMS technologies[16], where it is our future work.

## 4. Concluding remarks

In the present paper, the biocompatibility of fully self-contained implantable artificial cochlea which is made of P(VDF-TrFE) film, the Pt electrodes, and the Si substrate by MEMS and thin films technologies was studied by culturing cerebral cortical neurons from rats. The neurons were successfully cultured on the P(VDF-TrFE) film modified by the fibronectin and the collagen. From the phase contrast photographs, it was found that dendrites and an axon were extended from a soma of a neuron. No qualitative difference in terms of viability of neurons was found between the fibronectin and the collagen.

Furthermore, the neurons were successfully cultured over the P(VDF-TrFE) film and the Pt thin film electrode for the implantable artificial cochlea. Consequently, it was confirmed that the MEMS fabricated P(VDF-TrFE) films and implantable artificial cochlea were no cytotoxic effects on cultured neurons. The results presented here would provide the useful suggestions for further development of artificial organs research.

## Acknowledgements

The authors would like to thank Dr. Yoichi Kagaya, Mr. Yohei Nakamoto, and Mr. Toshiya Kanbe, Graduate School of Engineering Science, Osaka University, for their technical support.

## References

(1) Lewandowski, B.E., Kilgore, K.L., and Gustafson, K.J., Design considerations for an implantable, muscle powered piezoelectric system for generating electrical power, *Annals of Biomedical Engineering*, Vol. 35, No. 4 (2007), pp.631-641.

(2) Platt, S.R., Farritor, S., Garvin, K., and Haider, H., The use of piezoelectric ceramics for electric power generation within orthopedic implants, *IEEE/ASME Transactions on Mechatronics*, Vol. 10, No.4 (2005), pp.455-461.

(3) Schubert, W., Baurschmidt, P., Nagel, J., Thull, R., and Schaldach, M., An implantable artificial pancreas, *Medical & Biological Engineering & Computing*, Vol. 18, No. 4 (1980), pp. 527-537.

(4) Schrag, H.J., Ruthmann, O., Doll, A., Goldschmidtböing, F., Woias, P., and Hopt, U.T., Development of a novel remote-controlled artificial bowel sphincter through microsystems technology, *Artificial Organs*, Vol. 30, No. 11 (2006), pp. 855-862.

(5) Shintaku, H., Tanujaya, H., Nakamoto, Y., Nakagawa, T., Kawano, S., and Ito, J., Fluid dynamical analysis on basic characteristics of MEMS fabricated artificial cochlea," *The Seventh JSME-KSME Thermal and Fluids Engineering Conference*, (2008), p.155 & CDROM.

(6) Shintaku, H., Tanujaya, H., Nakagawa, T., Ito, J., and Kawano, S., Acoustical frequency selectivity of piezoelectric artificial cochlea, *Proceedings of the 25th Sensor Symposium on Seonsors, Micromachines, and Applied Systems*, (2008), pp.847-848.

(7) Shintaku, H., Nakagawa, T., Kanbe, T., Tanujaya, H., Kawano, S., and Ito, J., Microfabricated acoustic sensor with frequency selectivity and electric signal conversion for novel artificial cochlear system, will be presented at *2009 JSME-IIP/ASME-ISPS Joint Conference on Micromechatronics for Information and Precision Equipment (MIPE 2009)* (2009), pp. 341-342.

(8) Spelman, F.A., The past, present, and future of cochlear prostheses, *IEEE Engineering in Medicine and Biology Magazine*, Vol. 18, No. 3 (1999), pp. 27-33.

(9) Zeng, F.G., Trends in cochlear implants, *Trends in Amplification*, Vol. 8, No. 1 (2004), pp. T1–T34.

(10) Waltzman, S.B., Cochlear implants: current status, *Expert Review of Medical Devices*, Vol. 3, No. 5 (2006), pp. 647–655.

(11) Kotzar, G., Freas, M., Abel, P., Fleischman, A., Roy, S., Zorman, C., Moran, J.M., and Melzak, J., Evaluation of MEMS materials of construction for implantable medical devices, *Biomaterials*, Vol. 23, No. 13 (2002), pp. 2737-2750.

(12) Yamada, K.M., and Olden, K., Fibronectins-adhesive glycoproteins of cell surface and blood, *Nature*, Vol. 275, No. 5677 (1978), pp. 179-184.

(13) Kleinman, H.K., Klebe, R.J., and Martin, G.R., Role of collagenous matrices in the adhesion and growth of cells, *The Journal of Cell Biology*, Vol. 88, No.3 (1981), pp. 473-485.

(14) Muramoto, K., Kobayashi, K., Nakanishi, S., Matsuda, Y., and Kuroda, Y., Functional synapse formation between cultured neurons of rat cerebral cortex, *Proceedings of the Japan Academy Series B*, Vol. 64, No. 10 (1988), pp.319-322.

(15) Quinn, B., Toga, A.W., Motamed, S., and Merlic, C.A., Fluoro Nissl Green: a novel fluorescent counterstain for neuroanatomy, *Neuroscience Letters*, Vol. 184, No. 3 (1995), pp. 169-172.

(16) Ostuni, E., Kane, R., Chen, C.S., Ingber, D.E., and Whitesides, G.M., Patterning mammalian cells using elastomeric membranes, *Langmuir*, Vol.16, No. 20 (2000), pp. 7811-7819.